International Journal for Numerical Methods in Engineering

WILEY

RESEARCH ARTICLE

An Optimized Algorithm for the Mitigation of Numerical Oscillations in Engineering Simulations: A Case Study in Grain Aeration Modeling

Daniel Rigoni[1,2] | Marcio Augusto Villela Pinto[3] | Jotair Elio Kwiatkowski Jr.[1]

[1]Department of Computer Science, State University of Central-West (UNICENTRO), Guarapuava, Brazil | [2]Graduate Program in Numerical Methods in Engineering, Federal University of Paraná (UFPR), Curitiba, Brazil | [3]Department of Mechanical Engineering, Federal University of Paraná (UFPR), Curitiba, Brazil

Correspondence: Daniel Rigoni (danielrigoni@unicentro.br)

Received: 16 November 2025 | **Revised:** 14 January 2026 | **Accepted:** 24 February 2026

Keywords: artificial viscosity | computational efficiency | coupled systems | finite-difference | post-harvest | verification and validation

ABSTRACT

Spurious oscillations are a recurring challenge in numerical simulations of advection-dominated transport, often degrading stability and predictive accuracy. Artificial viscosity is commonly employed to mitigate these effects, but its coefficient is usually tuned empirically, limiting reproducibility and scalability. This study introduces a predictive framework in which the viscosity coefficient is derived analytically from discretization parameters through a closed-form law obtained via offline optimization guided by a smoothness metric. The methodology is demonstrated for grain aeration, a coupled heat-moisture transport problem of high practical relevance. The mathematical model was solved using finite differences with the Leith scheme, known for enhanced robustness under realistic aeration conditions. Verification based on apparent order-of-convergence analysis of the discretization error confirmed that the stabilized formulation recovered second-order accuracy, while the unstabilized model exhibited order degradation. Validation against experimental data showed accuracy comparable to manual calibration but with greater stability. Smoothness analysis revealed oscillations only in the energy balance, with mass-balance equations remaining naturally smooth. Once trained, the predictive law added negligible computational cost (3.5 s per run vs. 162.1 s for mesh refinement - a well-known technique for reducing oscillations in numerical solutions). The approach eliminates empirical tuning, ensures convergence under experimental conditions, and achieves substantial computational savings for coupled transport problems.

1 | Introduction

Numerical modeling has become an indispensable instrument in engineering analysis and prediction, enabling the investigation of complex systems while reducing dependence on costly or impractical experimentation. Nevertheless,

despite its widespread adoption, the reliability of numerical simulations remains constrained by fundamental deficiencies associated with discretization. In particular, advection-dominated problems are prone to the emergence of spurious oscillations, which are most pronounced near steep gradients [1]. These artifacts do not originate from inadequacies in the governing equations, but rather from intrinsic limitations of numerical schemes, and their presence can compromise both the accuracy and the practical applicability of computational models [2].

Two principal strategies have traditionally been employed to mitigate numerical instabilities. The first—systematic mesh refinement—aims to reduce numerical dispersion by increasing spatial and temporal resolution. While conceptually straightforward, this approach becomes computationally prohibitive in practice, since the cost tends to scale superlinearly with problem size and can rapidly escalate [3]. The second strategy is the introduction of artificial viscosity, wherein controlled dissipation is added to suppress high-frequency oscillations and promote stability. Although it has been widely adopted, this method typically depends on empirically tuned viscosity coefficients, adjusted via trial-and-error procedures or fitted to experimental data, which limits generalization and reproducibility [4].

Prakash and Zhang [5] demonstrate that artificial viscosity coefficients introduced as closure terms are typically identified through dedicated offline calibration or optimization procedures based on high-fidelity data, prior to efficient online simulations. This observation reinforces the view that stabilization parameters are rarely universal and that their determination often represents a significant computational bottleneck.

Furthermore, most stabilization techniques are still tested on simplified problems, which fail to capture the nonlinear coupling of realistic systems. Methods that perform well in such idealized benchmarks often lose stability or require retuning in practical applications, while quantitative validation against experimentally calibrated data remains rare [6–8].

The present study addresses these limitations by reformulating artificial viscosity as a predictive coefficient derived directly from discretization parameters rather than empirical calibration. An offline optimization guided by a smoothness metric objectively quantifies oscillatory behavior and yields a closed-form predictive law. Once established, this law computes viscosity automatically and at negligible cost, ensuring stabilization without manual intervention.

The methodology is assessed in the context of grain aeration, a key post-harvest technique used to preserve quality and extend the storage life of bulk grains. Its effectiveness directly affects food security and economic sustainability, as inadequate control of thermal and moisture conditions can lead to severe quantitative and qualitative losses [9]. Physically, aeration involves coupled transport mechanisms—convective heat exchange, moisture migration, and air-grain interactions—that operate simultaneously in transient and heterogeneous environments. This makes aeration a problem of both practical relevance and high physical complexity, where predictive simulations play a decisive role in guiding engineering decisions.

The process is commonly represented by mathematical models describing the coupled transfer of heat and moisture within the grain mass. Among these, the model proposed by [10] remains one of the most widely used [11–15], balancing physical realism and computational efficiency. As no analytical solution is available, the model is solved numerically, typically using finite differences. Recent studies have shown that the Leith scheme [16] further enhances robustness under realistic aeration parameters, reinforcing its suitability for practical applications [15].

Despite these advances, the mathematical model remains prone to numerical difficulties: steep gradients develop as thermal and moisture fronts propagate through the bulk, and the strong coupling between transport processes exacerbates the susceptibility to spurious oscillations. Studies such as those reported by [14, 15] have shown that these oscillations can significantly distort the predicted propagation of thermal fronts, directly undermining the reliability of the model in practical scenarios. These characteristics make grain aeration an especially stringent benchmark for stabilization strategies, since discretization errors can compromise both numerical accuracy and engineering outcomes.

The contributions of this paper can be grouped into two complementary ideas. On the methodological side, a smoothness metric is introduced as an objective diagnostic for quantifying spurious oscillations, replacing subjective or qualitative assessments. In addition, artificial viscosity is reformulated from an empirically adjusted coefficient into a predictive parameter derived directly from discretization, thereby eliminating dependence on case-specific calibration and enhancing generality and reproducibility. These contributions establish a systematic and theoretically grounded approach to stabilization, addressing long-standing limitations in the literature.

On the applied side, a rigorous comparative framework is established in which the predictive methodology is contrasted with both uncontrolled instability and the benchmark of manual calibration against experimental data. Validation of the proposed approach is carried out using experimental results reported in the literature [17], ensuring that the conclusions extend beyond numerical analysis to conditions of practical relevance. A further contribution lies in the verification procedure itself, which is conducted rigorously over all points of the discrete domain rather than at selected locations, thus providing a more comprehensive and demanding assessment of numerical accuracy. In addition, a detailed analysis of computational complexity is performed, demonstrating that the predictive law achieves accuracy comparable to empirical calibration while requiring negligible additional cost. The objective is to demonstrate that the methodology not only preserves stability and accuracy but also offers substantial efficiency gains relative to mesh refinement and manual tuning, thereby underscoring its potential for application in large-scale engineering simulations.

The remainder of this paper is organized as follows. Section 2 introduces the mathematical formulation of the aeration model, together with the governing parameters and the experimental dataset employed for validation. Section 3 describes the numerical discretization, the definition of the smoothness metric, and the optimization procedure through which the predictive law for artificial viscosity is derived. Section 4 presents the results of numerical verification, experimental validation, and comparative analyses, with particular emphasis on computational efficiency. Finally, Section 5 concludes the paper by summarizing the main findings.

2 | Mathematical Model and Experimental Framework

The development and evaluation of numerical methods are often conducted on simplified equations such as linear advection or advection—diffusion models. Although these canonical formulations provide valuable theoretical insight, their simplicity rarely exposes the difficulties encountered in realistic applications [18]. For example, numerical schemes that perform well under idealized conditions may require substantial modification or fail altogether when extended to fully coupled nonlinear problems [19, 20]. Similar limitations have been observed across disciplines, where validation is frequently restricted to idealized or synthetic datasets, offering limited evidence of robustness in truly complex systems [21, 22].

In this context, the present study adopts grain aeration as a representative case study, deliberately avoiding canonical benchmarks. This problem combines practical importance in post-harvest preservation with significant numerical challenges, involving coupled heat and mass transfer under realistic boundary and initial conditions. Its nonlinear and transient nature provides a stringent yet meaningful test for evaluating the robustness and generality of the proposed stabilization algorithm. This section presents the mathematical formulation of the grain aeration problem.

2.1 | Governing Equations

The grain aeration process is governed by partial differential equations describing the transport of heat, moisture, and air. These equations arise from the principles of conservation of energy and mass, together with constitutive relations that link temperature, water content, and airflow in the porous medium. The original formulation was presented in detail by [10], and later studies demonstrated that certain simplifications could be introduced without loss of accuracy [11]. That simplified version has since been widely adopted in investigations of grain storage and aeration [12–15], and it is the formulation adopted in this paper.

The energy balance for the grain bulk accounts for heat storage in both the kernels and the intergranular air, convective transport driven by the airflow, and heat exchange due to biological activity. In compact form, the temperature field is governed by:

$$\frac{\partial T}{\partial t}\left\{\rho_\sigma[c_g + c_W U] + \varepsilon\rho_a\left[c_a + R\left(c_W + \frac{\partial h_v}{\partial T}\right)\right]\right\} = \rho_\sigma h_s \frac{\partial U}{\partial t} - u_a\rho_a\left[c_a + R\left(c_W + \frac{\partial h_v}{\partial T}\right)\right]\frac{\partial T}{\partial y} + \rho_\sigma \frac{dm}{dt}(Q_r - 0.6h_v), \tag{1}$$

where t is time (s), y is the vertical coordinate oriented from bottom to top (m), T is grain temperature (°C), U is grain moisture content (kg kg^{-1}), u_a is the aeration air velocity (m s^{-1}), c_g, c_W, and c_a are the specific heats of grain, water, and

air, respectively (J kg^{-1} °C^{-1}), R is the air humidity ratio (kg kg^{-1}), ρ_a is the density of intergranular air (kg m^{-3}), ρ_σ is the grain bulk density (kg m^{-3}), h_v is the latent heat of vaporization of water (J kg^{-1}), h_s is the differential heat of sorption (J kg^{-1}), ϵ is grain porosity (decimal), dm/dt is the dry matter loss rate (kg s^{-1}), and Q_r is the heat of oxidation due to respiration (J s^{-1} m^{-3}).

Moisture transfer is described by a complementary mass balance:

$$\rho_\sigma \frac{\partial U}{\partial t} = -u_a \rho_a \frac{\partial R}{\partial y} + \frac{dm}{dt}(0.6 + U). \tag{2}$$

The energy equation depends on the moisture content, since both the effective heat capacity and the sorption term involve U. In turn, the moisture equation depends on the humidity ratio R, which is a function of temperature T and moisture U. As a result, heat and mass transfer cannot be treated independently: variations in temperature affect moisture redistribution, and changes in moisture alter the thermal properties of the bulk. This interdependence is a defining characteristic of grain aeration and is central to the challenges addressed in this work.

The humidity ratio R is defined as the mass of water vapor per unit mass of dry air in a given mixing volume. In the aeration model, R links air psychrometrics to the coupled heat-moisture dynamics in the grain bulk, enabling consistent estimation of water content and the expected effects of aeration on storage conditions. Following [23], it can be computed as

$$R = 0.622 \, \frac{r_u \, p_s}{P_{atm} - r_u \, p_s}, \tag{3}$$

where P_{atm} is the atmospheric pressure (kPa), p_s is the saturation vapor pressure (kPa), and r_u is the equilibrium relative humidity (in decimal).

The saturation vapor pressure p_s may be expressed as [24]

$$p_s = \frac{6 \times 10^{25}}{1000 \, (T + 273.15)^5} \exp\left(-\frac{6800}{T + 273.15}\right), \tag{4}$$

and the equilibrium relative humidity r_u can be evaluated using [25]

$$r_u = 100 \, \exp\left[-\frac{A}{T + C} \, \exp(-B \, U)\right], \tag{5}$$

where A, B, and C are material-dependent empirical constants. Equations (3–5) make explicit the coupling: R depends on r_u and p_s, both of which are temperature-dependent, and r_u further depends on the grain moisture U; consequently, the moisture and energy balances are linked through $R(T, U)$.

The procedures for calculating the parameters in Equations (1–5), as well as the alternative expressions reported for different grain types, are not presented here in detail. These formulations can be found in [14, 15], where the complete methodology is described. In the present study, the same methodology is followed to ensure consistency with those validated approaches.

It is worth noting that the formulation adopted is one-dimensional in space and transient in time. The vertical axis is taken as the direction of airflow, consistent with the dominant transport mechanism during aeration. The one-dimensional approximation has been widely used to capture the essential coupled dynamics of heat and moisture transfer in grain and porous media, offering satisfactory accuracy while keeping the computational cost manageable [26]. Although multidimensional formulations exist and can provide more detailed flow structures, reviews consistently highlight that one-dimensional models remain the most practical choice for engineering simulations where efficiency and robustness are key [27].

The current study considers an up-flow aeration system, where $y \in [0, L]$ and L denotes the height of the grain storage bin in meters. While the analysis is centered on a one-dimensional approach, Figure 1 illustrates a realistic three-dimensional bin to provide a clearer representation of the geometry and boundary conditions involved in the aeration process.

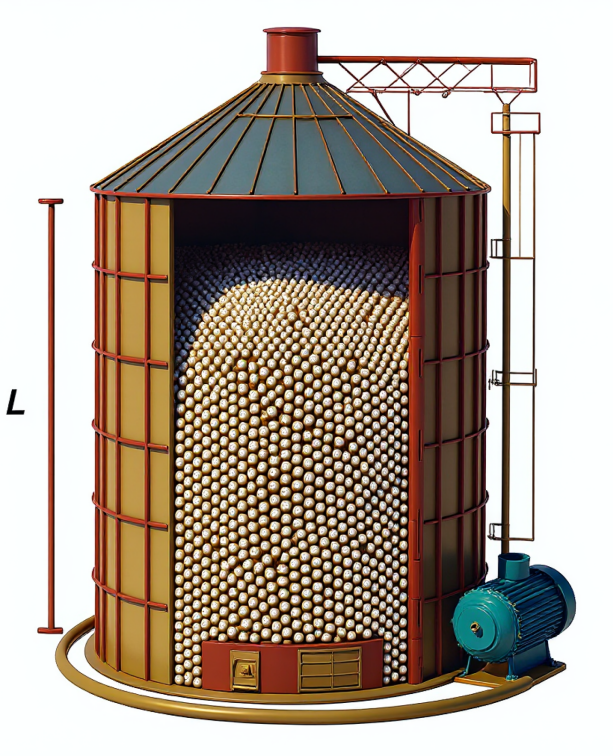

FIGURE 1 | Schematic of the up-flow aeration system: airflow is forced by a motor and fan unit installed at the bottom of the bin.

2.2 | Initial and Boundary Conditions

The solution of the governing equations requires appropriate boundary and initial conditions to represent the physical setup of the storage bin under aeration. In the present study, the aeration system is operated in up-flow mode, with air forced from the base upward by a motorized fan (see Figure 1).

At the bottom boundary ($y = 0$), the grains at the base of the bin are assumed to reach equilibrium with the aeration airflow. As a result, their temperature is prescribed to equal the temperature of the incoming air,

$$T(0,t) = T_B, \tag{6}$$

where T_B denotes the aeration air temperature.

The equilibrium moisture content of the grain at the base is computed through an adaptation of the Chung–Pfost relation, which links grain sorption characteristics to air humidity and temperature [25]

$$U(0,t) = -\frac{1}{B}\ln\left[\ln\left(-\frac{r_a}{100}\right)\left(-\frac{T_B + C}{A}\right)\right] = U_B, \tag{7}$$

where U_B is the equilibrium moisture content and r_a is the relative humidity of the aeration airflow. The latter is not necessarily equal to the ambient humidity, but is influenced by differences between the ambient and inlet air temperatures. Following [23], it can be expressed as

$$r_a = u_r \frac{K_1 \exp(K_2 - K_4)}{K_3}, \tag{8}$$

where u_r is the ambient relative humidity and the coefficients are

$$K_1 = \frac{6\times 10^{25}}{1000(T_{\text{amb}} + 273.15)^5}, K_2 = -\frac{6800}{T_{\text{amb}} + 273.15}, K_3 = \frac{6\times 10^{25}}{1000(T_B + 273.15)^5}, K_4 = -\frac{6800}{T_B + 273.15}. \tag{9}$$

These expressions highlight that the inlet moisture conditions are intrinsically dependent on both ambient and aeration temperatures, reinforcing the coupling between airflow characteristics and grain state.

At the top of the domain ($y = L$), homogeneous Neumann conditions are applied for both temperature and moisture:

$$\left.\frac{\partial T}{\partial y}\right|_{y=L} = \left.\frac{\partial U}{\partial y}\right|_{y=L} = 0, \tag{10}$$

allowing heat and vapor to leave the system without imposing artificial gradients. Physically, this represents the free outflow of air after it has traversed the grain mass.

Initial conditions are assumed uniform throughout the domain. The initial temperature corresponds to the bulk condition of the grain immediately after drying:

$$T(y, 0) = T_I, \tag{11}$$

where T_I is the initial grain temperature.

Likewise, the initial moisture content is determined from the post-drying percentage U_p, which is conventionally expressed on a wet basis (w.b.). In this convention, moisture corresponds to the ratio of water mass to the total mass of the grain sample (water plus dry matter):

$$U_{w.b.} = \frac{m_w}{m_w + m_d} \times 100, \tag{12}$$

where m_w is the water mass and m_d is the dry matter mass. While this definition is commonly used in experimental reporting, numerical models of grain storage typically adopt a dry basis (d.b.) formulation, in which moisture is expressed relative only to the dry matter:

$$U_{d.b.} = \frac{m_w}{m_d}. \tag{13}$$

The relationship between the two conventions is straightforward:

$$U_{d.b.} = \frac{U_{w.b.}}{100 - U_{w.b.}}. \tag{14}$$

Accordingly, the initial condition for the model is defined as

$$U(y, 0) = \frac{U_p}{100 - U_p} = U_I, \tag{15}$$

where U_p is the post-drying moisture content expressed on a wet basis (%), and U_I is the corresponding dimensionless moisture content on a dry basis used in the simulations.

Together, Equations (11–15) define a consistent initial–boundary value problem for the aeration process. The conditions ensure that the model captures the influence of the incoming airflow, the storage geometry, and the state of the grain after drying, thereby providing a realistic starting point for the transient simulations.

Due to the inherent complexity of the model, no closed-form analytical solutions are available. The system involves nonlinear source terms, strong coupling between temperature, moisture content, and humidity ratio, and boundary conditions that depend explicitly on ambient air properties. These characteristics preclude the derivation of exact analytical expressions. Consequently, analytical benchmarks such as those used for advection or diffusion equations cannot be employed here. Instead, validation and assessment of the numerical methodology must rely on numerical verification techniques and comparison with experimental data reported in the literature.

To enhance clarity, consistency, and reproducibility, Appendix A collects the complete nomenclature and concise definitions of all variables used in the governing equations.

2.3 | Experimental Data

To validate the numerical methodology, experimental data from grain aeration tests were considered. These data include measurements of the grain temperature profile during forced-air ventilation, together with records of inlet air

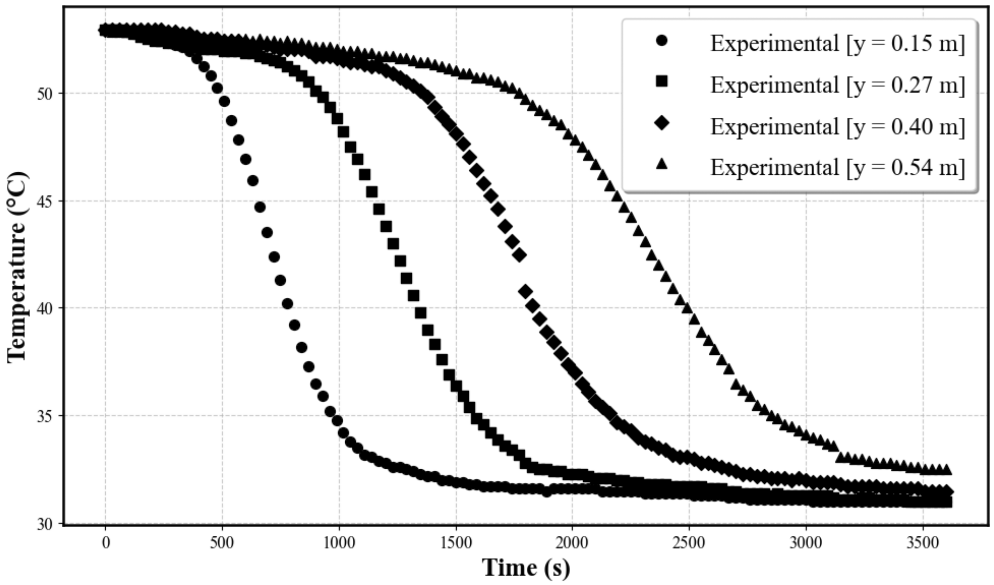

FIGURE 2 | Experimental grain temperature profiles at heights of 0.15, 0.27, 0.40, and 0.54 m during one hour of aeration [17].

temperature, ambient relative humidity, and airflow rate. Such variables provide the necessary boundary conditions for the model, as well as the reference values against which the simulated results can be compared.

The framework was based on the protocols reported by [17], conducted at the Laboratory of Physical Measurements and Mathematical Modeling at the Regional University of Northwest Rio Grande do Sul, Brazil. The experiments were carried out in a prototype bin constructed from a PVC tube with thermally insulated lateral walls. The storage column measured 1.0 m in height ($L = 1$ m) and 0.15 m in diameter. Soybeans were used as the test material, with an average initial moisture content of 12% (w.b.) and preheated to approximately 52.9°C prior to the aeration process. The aeration air was supplied at a constant temperature of 31.1°C, driven by a fan at the base of the bin.

Temperature monitoring was performed using thermocouples installed at four distinct heights within the grain bulk: 0.15, 0.27, 0.40, and 0.54 m. Measurements were recorded at 30-second intervals over a one-hour aeration period, capturing the transient behavior of the grain temperature profile. The resulting data are presented in Figure 2 and represent the empirical benchmark for assessing the predictive capability of the model.

Importantly, the experimental dataset is not employed for parameter calibration. Instead, it serves exclusively as an independent benchmark for validation, enabling a direct and objective comparison between simulated and observed grain temperature and moisture dynamics. By reproducing the operating conditions of the aeration test and assessing the degree of agreement between numerical predictions and experimental outcomes, the study establishes a rigorous test of model reliability. This strategy elevates the validation beyond a simple numerical exercise: it demonstrates that the proposed methodology not only yields accurate solutions but also maintains predictive capability under realistic post-harvest storage conditions. In doing so, it highlights the potential of the model as a practical and robust tool for engineering applications.

For completeness and transparency, Appendix A reports the full set of model parameters adopted in the validation study, which are selected to match the experimental conditions described above, including the physical and thermodynamic values corresponding to soybeans, thereby ensuring consistency between the numerical simulations and the experimental configuration.

3 | Numerical Formulation and Algorithm

In this study, the finite difference method is adopted to discretize both space and time, a choice that is widely recognized in the literature for its clarity and effectiveness in heat and mass transfer problems [28]. The organization of the numerical formulation follows a systematic structure. First, the discretization schemes employed to approximate the governing equations are presented. Next, the role of artificial viscosity in stabilizing oscillatory solutions is examined, together with

a discussion of traditional approaches to defining the viscosity factor. Building on this basis, the proposed algorithm is introduced, in which a smoothness metric is used to quantify nonphysical oscillations and an optimization process derives a predictive relation for the artificial viscosity factor as a function of grid resolution. Finally, the test scenarios used to evaluate the methodology are described, establishing the foundation for the comparative analyses that follow.

3.1 | Numerical Model

To approximate the equations governing grain aeration, the computational domain is discretized in both space and time. The vertical coordinate is defined as $y \in [0, L]$ and divided into N_y equally spaced nodes, yielding a mesh size of

$$\Delta y = \frac{L}{N_y - 1}.$$

In the temporal direction, the total simulation time t_f is partitioned into N_t steps of size

$$\Delta t = \frac{t_f}{N_t}.$$

Thus, the solution is advanced step by step in time, while the state variables are evaluated at each spatial node along the grain column. For convenience, each spatial node is identified by its relative position in the mesh: the central node of interest is denoted by P, with its immediate neighbors represented by S (south, below) and N (north, above). In the temporal domain, discrete time levels are labeled by n and $n+1$, corresponding to the current and next time steps, respectively. In practice, this corresponds to slicing the grain column into N_y layers and updating their states through N_t successive instants, capturing the evolution of temperature and moisture during the aeration process.

Before introducing the discretization procedure, it is convenient to rewrite the governing equations in a simplified form. This reformulation groups the physical parameters into effective coefficients, highlighting the role of each term in the dynamics of the problem.

The grain temperature equation (Equation 1) can thus be expressed as

$$C_T \frac{\partial T}{\partial t} = D_T \frac{\partial U}{\partial t} - v_T \frac{\partial T}{\partial y} + S_T, \tag{16}$$

where the effective coefficients are defined as

$$C_T = \rho_\sigma \left(c_g + c_W U\right) + \varepsilon \rho_a \left[c_a + R\left(c_W + \frac{\partial h_v}{\partial T}\right)\right], \tag{17}$$

$$D_T = \rho_\sigma h_s, \tag{18}$$

$$v_T = u_a \rho_a \left[c_a + R\left(c_W + \frac{\partial h_v}{\partial T}\right)\right], \tag{19}$$

$$S_T = \rho_\sigma \frac{dm}{dt}\left(Q_r - 0.6 h_v\right), \tag{20}$$

where C_T is the effective thermal capacity of the grain–air system, D_T is the coupling coefficient linking temperature to changes in moisture, v_T is the effective advective transport coefficient associated with the aeration airflow, and S_T is the source term representing respiration and oxidation heat release.

Similarly, the grain moisture equation (Equation 2) can be simplified to

$$C_U \frac{\partial U}{\partial t} = - v_U \frac{\partial R}{\partial y} + S_U, \tag{21}$$

where

$$C_U = \rho_\sigma, \tag{22}$$

$$v_U = u_a \rho_a, \tag{23}$$

$$S_U = \frac{dm}{dt}\,(0.6 + U)\,. \tag{24}$$

It is important to note that $R = R(T, U)$, so that the gradient $\partial R/\partial y$ preserves the coupling between temperature and moisture in the discrete formulation, in line with the physical interactions described in Section 2.

As mentioned in previous work [15], the scheme presented by [16] has been shown to be considerably more robust than other discretization methods when applied to the aeration model under study. Building on this result, the present work adopts the Leith Scheme (LS) to approximate the temporal and spatial derivatives of the governing equations.

For the temperature equation (Equation 16), the LS approximates the derivatives at point P as follows:

$$\left(\frac{\partial T}{\partial t}\right)_P^{n+1} \approx \frac{T_P^{n+1} - T_P^n}{\Delta t}, \tag{25}$$

$$\left(\frac{\partial T}{\partial y}\right)_P^{n+1} \approx \tau\,\frac{T_P^n - T_S^n}{\Delta y} + (1-\tau)\,\frac{T_N^n - T_S^n}{2\Delta y}, \tag{26}$$

where

$$\tau = \frac{v_T}{C_T}\,\frac{\Delta t}{\Delta y}. \tag{27}$$

Substituting into Equation (16), the discretized temperature equation becomes

$$T_P^{n+1} = (1-\tau^2)T_P^n + \frac{1}{2}(\tau^2+\tau)\,T_S^n + \frac{1}{2}(\tau^2-\tau)\,T_N^n + \frac{\Delta t}{C_T}\left(D_T\frac{\partial U}{\partial t} + S_T\right). \tag{28}$$

Similarly, the grain moisture equation (Equation 21) is discretized as

$$U_P^{n+1} = \alpha\,U_P^n - \beta\left(\frac{\partial R}{\partial y}\right)_P^n + \frac{\Delta t}{C_U}\,S_U, \tag{29}$$

with coefficients defined by

$$\alpha = \frac{2C_U}{2C_U - \Delta t\,\frac{dm}{dt}}, \qquad \beta = \left(\frac{v_U}{C_U}\,\frac{\Delta t}{\Delta y}\right)^2. \tag{30}$$

At the upper boundary ($y = L$), Neumann conditions are imposed using the ghost-point technique [28], resulting in

$$T_{N_B}^{n+1} = T_{N_B}^n + \frac{\Delta t}{C_T}\left(D_T\frac{\partial U}{\partial t} + S_T\right), \tag{31}$$

$$U_{N_B}^{n+1} = \left(1 + \frac{\Delta t}{C_U}\frac{dm}{dt}\right)U_{N_B}^n + \frac{0.6\,\Delta t}{C_U}\frac{dm}{dt}. \tag{32}$$

Because the LS adopted here is explicit [29], no algebraic system is solved at each step, which keeps the implementation lightweight. A Courant-type parameter naturally arises,

$$\tau \;=\; \frac{v_T}{C_T}\,\frac{\Delta t}{\Delta y},$$

with C_T and v_T given by Equations (17–19). In grain aeration, the effective capacity C_T dominates the advective coefficient v_T over the relevant operating range (the temporal scale is much stiffer than the spatial transport scale). Consequently, for the Δt and Δy used here, one consistently obtains $\tau \ll 1$, ensuring practical stability without restrictive time steps; claims of unconditional stability are thus unnecessary for this model class. It should also be emphasized that the observed oscillations do not stem directly from the explicit discretization itself. Previous studies employing central difference schemes with Crank–Nicolson time integration for the same aeration model also reported oscillatory behavior [14, 15], indicating that spurious oscillations are inherent to the advection-dominated character of the problem rather than to the choice of explicit time stepping.

3.2 | Artificial Viscosity

A well-known difficulty in the numerical solution is the appearance of nonphysical oscillations, particularly when sharp gradients are present in the solution. In the context of grain aeration modeling, such oscillations may manifest in the profiles of temperature, leading to unrealistic predictions [14]. These artefacts are not related to the physical processes of the system, but rather to the discretization of advective terms on a finite grid.

To mitigate these spurious oscillations, Artificial Viscosity (AV) is commonly introduced into the discrete equations [30–33]. The underlying idea is to add a dissipative term that damps high-frequency components of the numerical solution, thereby restoring stability without compromising the essential features of the physical process. In the literature, AV has been widely adopted in computational fluid dynamics and porous media transport problems, often proving to be an effective stabilization tool [34].

Originally proposed by [32], AV modifies the flux of the Partial Differential Equation (PDE) by introducing a dissipative correction. The discretized AV term can be expressed as [14]

$$\frac{\partial}{\partial y}\left[\mu(\Delta y)^2\left|\frac{\partial T}{\partial y}\right|\frac{\partial T}{\partial y}\right] \approx \frac{\mu}{\Delta y}\left[\left|T_N^n - T_P^n\right|\left(T_N^n - T_P^n\right) - \left|T_P^n - T_S^n\right|\left(T_P^n - T_S^n\right)\right]. \tag{33}$$

Substituting the discretized AV term (Equation 33) into the numerical formulation of temperature (Equation 28), the temperature equation with AV becomes

$$\begin{aligned} T_P^{n+1} = (1-\tau^2)T_P^n + \frac{1}{2}(\tau^2+\tau)\,T_S^n + \frac{1}{2}(\tau^2-\tau)\,T_N^n + \frac{\Delta t}{C_T}\left(D_T\frac{\partial U}{\partial t} + S_T\right) \\ + \frac{\mu}{\Delta y}\left[\left|T_N^n - T_P^n\right|\left(T_N^n - T_P^n\right) - \left|T_P^n - T_S^n\right|\left(T_P^n - T_S^n\right)\right]. \end{aligned} \tag{34}$$

Traditionally, the choice of the artificial viscosity factor (μ) is made either heuristically, by trial and error, or through extensive calibration against experimental data [30, 35]. In some cases, manual parameter sweeps are performed, where μ is varied over several orders of magnitude until oscillations are suppressed while minimizing excessive numerical diffusion. Although this procedure can lead to acceptable results, it is computationally expensive and lacks generality, since the optimal factor is strongly dependent on the mesh resolution and the specific problem under study [36, 37].

The limitations of these traditional approaches motivate the development of an adaptive strategy for defining μ. In this work, AV is not treated as an external tuning parameter, but rather as a quantity that can be predicted from the properties of the grid and the dynamics of the solution itself. The following subsection introduces the proposed algorithm that formalizes this idea, providing a systematic way to compute μ adaptively during the simulation process.

3.3 | Proposed Algorithm

A key innovation of this work lies in the introduction of an adaptive algorithm that automatically determines the artificial viscosity factor μ. Rather than relying on trial-and-error calibration or manual parameter sweeps, the proposed method computes μ directly from the simulation, ensuring robustness across different spatial and temporal resolutions. The approach is built on three essential components: a smoothness metric to quantify oscillations, an optimization process to determine the optimal viscosity, and a predictive equation that generalizes these findings for any grid configuration.

3.3.1 | Smoothness Metric

A fundamental step in the proposed algorithm is the definition of a smoothness metric, denoted by σ, which quantifies the degree of spurious variation in the numerical solution. The evaluation of σ is performed locally at each time step and then aggregated over the domain, providing a global assessment of the solution stability.

A recurring challenge in advection-dominated problems is the emergence of nonphysical oscillations in regions where the solution should remain smooth, typically arising from the discretization of advective terms rather than from physical effects. While mesh refinement is a common practice to mitigate such artefacts, this approach can be prohibitively expensive in engineering problems, where the number of spatial and temporal nodes directly impacts computational cost

[38]. Instead of relying on increasingly fine meshes, the present work introduces a smoothness-based criterion that quantifies oscillations and guides the application of AV. This allows oscillations to be suppressed adaptively without excessive refinement, thereby achieving stability at a fraction of the computational cost.

The core idea is to quantify the local variability of the numerical profile relative to its expected physical behavior. For monotonic cases, given a discrete temperature distribution $\{T_j^n\}_{j=1}^{N_y}$ at time step n, the smoothness metric is defined as

$$\sigma^n = \sum_{j=1}^{N_y-1} \left(T_{j+1}^n - T_j^n\right)^2, \tag{35}$$

where the summation accounts for all nearest-neighbor differences along the grain column. Oscillatory profiles, characterized by frequent sign changes in the discrete gradient, yield large values of σ^n, whereas smooth profiles with consistent gradients result in smaller values.

To ensure robustness, the smoothness metric is aggregated over both the temporal and spatial domains, giving a global indicator of oscillations:

$$\sigma = \sum_{n=n_0}^{n_0+N_t^*-1} \sum_{j=1}^{N_y-1} \left(T_{j+1}^n - T_j^n\right)^2, \tag{36}$$

where the inner summation measures variability across neighboring spatial nodes at each time step, while the outer summation accumulates this variability across a window of N_t^* time steps.

This aggregation reduces the influence of transient fluctuations and provides a stable global indicator of numerical stability. The advantage of this formulation is twofold. First, it is computationally inexpensive, requiring only $\mathcal{O}(N_y)$ operations per time step and negligible additional storage. Second, it directly targets the numerical artefacts that most compromise the physical interpretability of the results. By coupling σ with the artificial viscosity factor μ, the algorithm automatically selects the minimal amount of dissipation required to suppress oscillations. This eliminates the need for manual parameter sweeps or costly mesh refinement, enabling the model to be applied efficiently to realistic grain aeration scenarios.

To highlight the behavior of the smoothness metric over time, consider, for example, two consecutive time steps of the temperature profile with $N_y = 5$ nodes.

At time step n, assume a smooth and an oscillatory solution, respectively given by

$$T^n = \{50,\ 48,\ 46,\ 44,\ 42\} \text{ and } \overline{T}^n = \{50,\ 52,\ 45,\ 47,\ 42\}.$$

At the following time step $n+1$, both profiles evolve further. The smooth case preserves monotonic behavior,

$$T^{n+1} = \{49,\ 47,\ 45,\ 43,\ 41\},$$

whereas the oscillatory case amplifies the spurious wiggles,

$$\overline{T}^{n+1} = \{49,\ 53,\ 44,\ 48,\ 41\}.$$

Evaluating the smoothness metric using Equation (35) gives

$$\sigma^n_{\text{smooth}} = 16, \qquad \sigma^{n+1}_{\text{smooth}} = 16, \qquad \sigma^n_{\text{oscillatory}} = 57, \qquad \sigma^{n+1}_{\text{oscillatory}} = 73.$$

This example shows that, in physically consistent profiles, the smoothness metric remains low and stable over time, whereas in oscillatory profiles it not only starts high but tends to grow as spurious oscillations propagate or amplify [39]. To obtain a robust global measure, the metric can then be aggregated over a time window, as defined in Equation (36), providing a stable indicator of overall numerical stability across the full simulation. To formalize the computation of the smoothness metric, the step-by-step procedure is outlined in Algorithm 1.

At first sight, the definition in Equation (36)—a sum of squared first differences—does not explicitly count sign changes of the discrete gradient. One may wonder whether it would also penalize smooth but steep monotone fronts. In the aeration

ALGORITHM 1 | Computation of the Smoothness Metric (σ).

Input: Temperature field $\{T_j^n\}_{j=1}^{N_y}$ for N_t^* time steps
Initialise $\sigma \leftarrow 0$
for $n = n_0$ to $n_0 + N_t^* - 1$ **do**
    Initialise $\sigma^n \leftarrow 0$
    for $j = 1$ to $N_y - 1$ **do**
        Compute local difference $\Delta T \leftarrow T_{j+1}^n - T_j^n$
        Accumulate: $\sigma^n \leftarrow \sigma^n + (\Delta T)^2$
    end for
    Update global metric: $\sigma \leftarrow \sigma + \sigma^n$
end for
Output: Global smoothness metric σ

problem, however, the physics provides a crucial structural prior: the cooling front produces a monotone temperature decrease along y (negative discrete gradient) over long time windows. In this regime, spurious oscillations manifest as high-frequency "ripples" superimposed on an otherwise monotone profile.

The metric σ effectively captures this behavior for two reasons. First, when the expected gradient has fixed sign, any local back-and-forth wiggle necessarily increases the local variation energy $\sum_j (T_{j+1} - T_j)^2$ beyond what a smooth monotone front would produce; thus, the excess roughness created by oscillations is amplified by the quadratic aggregation. Second, the temporal aggregation in Equation (36) suppresses isolated transients and emphasizes persistent serrated patterns: oscillations that survive across multiple steps accumulate consistently, while genuine smooth fronts contribute quasi-stationary, lower values.

Alternative oscillation measures lead to the same practical decisions in this application. For completeness, the following indicators were also tested: (i) a total-variation metric $\mathrm{TV} = \sum_n \sum_j |T_{j+1}^n - T_j^n|$ [40, 41], (ii) a curvature-based metric $\sum_n \sum_j (T_{j+1}^n - 2T_j^n + T_{j-1}^n)^2$ [42, 43], and (iii) a sign-change counter $S = \sum_n \sum_j \left[(T_{j+1}^n - T_j^n)(T_j^n - T_{j-1}^n) < 0\right]$ [44, 45]. Across the grids reported here, these alternatives yielded qualitatively identical rankings of candidate solutions and selected the same μ_{opt}, while being more expensive to evaluate or more sensitive to measurement noise.

From a computational perspective, the evaluation of the smoothness metric is highly efficient. The calculation at each time step requires only $\mathcal{O}(N_y)$ operations, since it involves nearest-neighbor differences along the spatial direction. The global aggregation over a window of N_t^* time steps adds a multiplicative factor, yielding a total complexity of $\mathcal{O}(N_y N_t^*)$, which is negligible compared with the cost of solving the governing equations. Given its $\mathcal{O}(N_y N_t^*)$ cost, numerical robustness, and excellent empirical agreement with these surrogates, Equation (36) is adopted throughout.

Moreover, the algorithm does not demand additional storage beyond the existing temperature field, as the metric can be accumulated on-the-fly during the simulation. This means that its integration into the solver has virtually no overhead, while providing a practical tool to quantify and control spurious oscillations.

3.3.2 | Optimization Process and Predictive Equation

The determination of the optimal artificial viscosity factor is based on a systematic search guided by the smoothness metric. For each pair of discretization parameters (N_y, N_t), a range of candidate viscosity factors $\mu \in [\mu_{\min}, \mu_{\max}]$ is defined, with a chosen increment $\Delta\mu$. For each candidate, the governing equations are solved numerically, producing discrete fields of temperature T, moisture U, and humidity ratio R over the full spatial and temporal domain.

The smoothness metric $\sigma(\mu)$ is then computed across the entire domain using Equation (36), which penalizes oscillatory behavior by assigning higher values whenever spurious fluctuations are present in the numerical profile. The optimal viscosity factor is selected as

$$\sigma(\mu_{\mathrm{opt}}) = \min_{\mu \in \{\mu_{\min}, \ldots, \mu_{\max}\}} \{\sigma(\mu)\}, \tag{37}$$

ALGORITHM 2 | Optimization process and derivation of predictive equation.

Input: Discretization parameters (N_y, N_t), search range $[\mu_{\min}, \mu_{\max}]$, increment $\Delta\mu$, polynomial degree d
Initialize dataset $\mathcal{D} \leftarrow \varnothing$
for Each pair (N_y, N_t) in the study **do**
    for Each candidate μ in $[\mu_{\min}, \mu_{\max}]$ with step $\Delta\mu$ **do**
        Solve the discretized model (Equation 28–33) with viscosity factor μ
        Compute smoothness metric $\sigma(\mu)$ using Algorithm 1
    end for
    Select $\mu_{\text{opt}} = \min\{\sigma(\mu)\}$
    Store triplet $(N_y, N_t, \mu_{\text{opt}})$ into dataset $\mathcal{D}$
end for
Fit polynomial regression of degree d to $\mathcal{D}$: $\mu_{\text{Proposed}}(N_y, N_t) = f(N_y, N_t)$.
Output: Predictive equation $\mu_{\text{Proposed}}(N_y, N_t)$

corresponding to the smallest global oscillation measure for the respective N_y and N_t values. This process effectively automates the selection of μ, eliminating the need for manual parameter sweeps. By exploiting the smoothness criterion directly on the computed solution, the algorithm ensures that oscillations are suppressed adaptively.

The optimization procedure provides a collection of optimal viscosity factors μ_{opt} associated with different spatial and temporal discretizations (N_y, N_t), that is, a set of size M, where M represents the number of variations of N_y and N_t used. The goal of this step is to construct a predictive law that generalizes these results, enabling μ to be estimated directly from the grid parameters without the need for repeated parameter sweeps.

To this end, the dataset of triplets

$$\mathcal{D} = \{(N_{y,i}, N_{t,i}, \mu_{\text{opt},i})\}_{i=1}^{M},$$

is used to train a surrogate model relating (N_y, N_t) to the corresponding viscosity factor. Polynomial regression is adopted, whereby the predictor μ_{Proposed} is expressed as a linear combination of polynomial terms in N_y and N_t, up to a chosen degree d. The coefficients of the polynomial are estimated by least squares, minimizing the difference between the predicted and the observed optimal factors in $\mathcal{D}$.

This approach has two main advantages. First, it captures nonlinear dependencies between the grid resolution and the stabilization parameter, which are expected due to the interaction of numerical diffusion with both spatial and temporal discretizations. Second, once the coefficients are identified, the predictive law provides a closed-form expression

$$\mu_{\text{Proposed}} = f(N_y, N_t), \tag{38}$$

that can be evaluated at negligible cost for any discretization.

Different polynomial degrees (e.g., $d = 4,\ 6,\ 8$) are tested to balance model complexity and generalization. The final choice is based on predictive accuracy when reproducing the optimization results. In this way, the predictive equation $\mu_{\text{Proposed}}(N_y, N_t)$ eliminates the need for manual calibration or repeated searches, enabling the model to be applied directly to new grid configurations with robust stabilization. The optimization routine described above can be summarized in Algorithm 2, which details the procedure for identifying the optimal viscosity factor and deriving the predictive law $\mu_{\text{Proposed}}(N_y, N_t)$.

In terms of computational complexity, the offline optimization is dominated by repeatedly solving the discretized governing equations for different candidate values of the artificial viscosity factor μ. For a fixed discretization, a single simulation costs $\mathcal{O}(N_y N_t)$, since the solution must be advanced across N_t time steps while resolving N_y spatial degrees of freedom. A sweep over N_μ candidates in $[\mu_{\min}, \mu_{\max}]$ therefore leads to an overall offline cost of $\mathcal{O}(N_\mu N_y N_t)$.

Although solving the same PDE multiple times may seem excessive at first, this workflow is fully consistent with how transport-dominated engineering problems are typically studied. In grain aeration, as in many applications, practitioners routinely execute large sets of simulations while varying operating conditions and model parameters to identify robust

operating regimes before committing to field trials. The proposed procedure does not create a new burden of repeated runs; instead, it converts an unavoidable exploratory process into a systematic and reproducible step focused specifically on stabilization.

Absent a predictive stabilization rule, users are generally left with two unsatisfactory options. One is to run a single simulation with an ad hoc choice of μ, which commonly yields either residual oscillations or excessive numerical diffusion, forcing iterative refinement of the mesh or parameter values without clear criteria or guarantees of improvement. The other is to tune μ against experimental data; while this may produce a visually acceptable match, it ties the coefficient to a specific set of operating conditions and discretization choices, limiting transferability and undermining reproducibility.

The proposed method resolves this dilemma by concentrating the computational effort into a controlled, one-time learning stage whose sole purpose is to infer the mapping between grid resolution and the stabilization strength required to suppress spurious oscillations. Once the predictive law $\mu_{\text{Proposed}}(N_y, N_t)$ is obtained, subsequent simulations require no further optimization: μ is evaluated directly at $\mathcal{O}(1)$ cost, and the governing equations are solved only once per new configuration.

In this sense, the repeated offline simulations are not wasted computation, but a deliberate investment that replaces trial-and-error refinement and experiment-dependent tuning with a general, automatic, and reproducible stabilization strategy. The result is a workflow that aligns with engineering practice—where simulation campaigns precede field implementation—while providing a principled mechanism to select μ across discretizations and operating regimes.

3.3.3 | Spectral Smoothness Metric for Nonmonotonic Solutions

For problems whose physically admissible solutions are nonmonotonic or oscillatory, oscillation quantification must rely on scale separation rather than on local pointwise variations. In such regimes, physically meaningful oscillations may be present at resolved spatial scales, whereas numerical artifacts can manifest either as unresolved high-frequency oscillations or as excessive numerical diffusion. Consequently, smoothness indicators based solely on local gradient magnitude may lead to incorrect solution selection by favoring overly diffusive profiles. Spectral analysis provides a natural framework to distinguish between resolved physical oscillations and nonphysical numerical content and has long been employed in the analysis of dispersive errors and implicit filtering strategies [7, 46, 47].

Let T_j denote the discrete numerical solution defined on N_y spatial nodes, and let $\hat{T}_k$ be its discrete Fourier transform. A spectral smoothness metric is defined as the fraction of spectral energy contained in high-frequency modes,

$$\sigma_{\text{HF}} = \frac{\sum_{k=k_c}^{N_y/2} \left|\hat{T}_k\right|^2}{\sum_{k=0}^{N_y/2} \left|\hat{T}_k\right|^2}, \tag{39}$$

where k_c is a cutoff wavenumber separating physically resolved scales from unresolved numerical content. Following established practice in spectral resolution analysis and implicit large eddy simulation, only the lower portion of the resolvable spectral band is considered physically meaningful [7, 47, 48]. Accordingly, the cutoff is chosen as

$$k_c = 0.7\,\frac{N_y}{2}, \tag{40}$$

which retains approximately the lower 70% of the resolvable spectrum while isolating modes dominated by grid-scale numerical artifacts. The metric σ_{HF} is dimensionless and assumes values in the interval [0, 1], with larger values indicating a higher fraction of unresolved high-frequency energy.

To illustrate the behavior of the spectral smoothness metric in a regime characterized by pronounced physical oscillations, a discrete example is considered. A physically admissible reference profile exhibiting multiple resolved oscillations is defined as

$$T_j^{\text{ref}} = \Big[20.0,\ 22.8,\ 21.2,\ 24.5,\ 22.1,\ 25.0,\ 21.6,\ 23.9,\ 20.8,\ 22.7,\ 21.5\Big]. \tag{41}$$

This profile contains significant oscillatory behavior but remains smooth at the grid scale, representing a physically meaningful solution.

Two numerical solutions obtained under identical discretization parameters but with different stabilization levels are then examined. The first solution, denoted T_j^A, corresponds to an excessively diffusive numerical approximation,

$$T_j^A = \Big[20.0,\ 21.0,\ 22.0,\ 23.0,\ 23.5,\ 23.8,\ 23.5,\ 23.0,\ 22.4,\ 21.8,\ 21.2\Big], \tag{42}$$

in which the oscillatory structure of the physical solution has been artificially smoothed. The second solution, T_j^B, represents a numerically admissible approximation that preserves the physically resolved oscillatory behavior without introducing grid-scale noise,

$$T_j^B = \Big[20.0,\ 22.6,\ 21.4,\ 24.2,\ 22.3,\ 24.7,\ 21.9,\ 23.6,\ 21.0,\ 22.9,\ 21.7\Big]. \tag{43}$$

For this case, the local smoothness metric based on pointwise gradients yields $\sigma_M(T^{\text{ref}}) = 66.97$, $\sigma_M(T^A) = 4.76$, and $\sigma_M(T^B) = 47.95$. These values indicate that the local metric would incorrectly favor the excessively diffusive solution T_j^A due to its reduced gradient magnitude, despite its clear loss of physically meaningful oscillatory content.

In contrast, the spectral smoothness metric yields $\sigma_{\text{HF}}(T^{\text{ref}}) = 1.56 \times 10^{-3}$, $\sigma_{\text{HF}}(T^A) = 3.70 \times 10^{-5}$, and $\sigma_{\text{HF}}(T^B) = 1.15 \times 10^{-3}$. Although the excessively diffusive solution T_j^A exhibits the lowest value of σ_{HF}, this occurs as a result of artificial removal of resolved physical energy. The physically admissible numerical solution T_j^B, on the other hand, closely matches the spectral distribution of the reference profile, preserving oscillatory content while avoiding spurious high-frequency energy.

It is important to emphasize that the role of the reference profile in this context is not to represent an exact analytical solution. In practical applications, the true physical solution is generally unknown. Therefore, the reference profile can be defined in two practical ways. (i) It may be provided by a manufactured function, following the Method of Manufactured Solutions (MMS), which is widely used in computational fluid dynamics for verification studies. However, in practice, it can be difficult to design a manufactured function that closely resembles the expected physical curve while simultaneously exhibiting the specific behaviors of interest (e.g., a sharp front combined with smooth regions, realistic asymmetry, and controlled modal content). (ii) Alternatively, the reference may be obtained numerically by computing an essentially non-oscillatory solution on a highly refined mesh, typically using an upwind discretization; such "oscillation-free, grid-converged" solutions are commonly adopted in the literature as benchmarks.

Accordingly, the spectral smoothness metric is not interpreted as an absolute minimization criterion. Since the physically admissible solution is unknown, the objective is not to minimize σ_{HF} indiscriminately, but rather to identify the smallest artificial viscosity coefficient that effectively suppresses unresolved high-frequency content while preserving the oscillatory features encoded in the reference profile. As the viscosity parameter μ increases, $\sigma_{\text{HF}}(\mu)$ typically exhibits an initial rapid decrease associated with the removal of numerical oscillations, followed by a plateau where unresolved content has been eliminated, and finally a further decrease corresponding to excessive numerical diffusion and loss of resolved physical scales. The optimal viscosity coefficient μ_{opt} is therefore identified at the onset of this plateau, rather than at the global minimum of $\sigma_{\text{HF}}(\mu)$.

From an algorithmic standpoint, the introduction of the spectral smoothness metric does not require any structural modification of the numerical procedure. The time integration scheme, artificial viscosity formulation, and optimization framework remain unchanged. The only modification occurs in line 6 of Algorithm 2, where the smoothness indicator $\sigma(\mu)$ is evaluated: the local pointwise metric is replaced by the spectral energy-based measure $\sigma_{\text{HF}}(\mu)$ defined in this section, which is computed from the discrete Fourier transform of the numerical solution. The optimal artificial viscosity coefficient μ_{opt} is then identified by detecting the onset of the plateau in $\sigma_{\text{HF}}(\mu)$ following the same optimization procedure adopted in the monotonic case. The additional computational cost associated with the Fourier transform, which scales as $\mathcal{O}(N_y \log N_y)$ and is incurred only once per simulation, is negligible when compared to the overall cost of the time-marching solver.

3.4 | Test Scenarios

To evaluate the performance of the proposed methodology, three representative test scenarios are defined. These scenarios are designed to highlight the differences between neglecting AV, relying on manual calibration against experimental data, and employing the adaptive approach proposed in this work.

Since the grain aeration problem considered in this study is characterized by physically monotonic temperature profiles along the storage depth, the smoothness metric introduced in Section 3.3.2 is employed throughout the remainder of the paper. In this regime, any oscillatory behavior observed in the numerical solution is necessarily nonphysical and can be reliably interpreted as a numerical artifact. Consequently, the use of the monotonic smoothness metric provides an appropriate and effective criterion for stabilization and for identifying the optimal viscosity factor in all test scenarios analyzed below.

i. *No artificial viscosity* ($\mu = 0$): In this baseline case, the governing equations are solved without any stabilization. This scenario is useful to expose the intrinsic oscillatory behavior of the discretized model when sharp temperature gradients arise. It illustrates the necessity of a stabilization strategy for producing physically meaningful results.

ii. *Manually calibrated viscosity using experiments (benchmark)*: In this case, the viscosity factor μ is determined through manual calibration against experimental data. The value is chosen by iteratively adjusting μ until the simulated temperature profiles align with the observed measurements, suppressing oscillations while limiting excessive numerical diffusion. This represents the conventional benchmark in the literature. However, such calibration ties the model to a specific experimental setup and set of boundary conditions, making μ scenario-dependent and not transferable to different operating conditions or parameter variations. Consequently, while effective in reproducing one dataset, this approach lacks generality and can be impractical when multiple simulations are required.

iii. *Proposed adaptive viscosity* (μ_{Proposed}): In this scenario, the artificial viscosity is computed using the predictive law derived in Section 3.3. The factor $\mu_{\text{Proposed}}(N_y, N_t)$ is obtained directly from the grid parameters, eliminating the need for calibration or parameter sweeps. Unlike the experimental calibration strategy, this approach adapts naturally to different discretizations and model parameters, ensuring robust stability control without external tuning. The predictive formulation provides not only accuracy comparable to the benchmark but also scalability for new scenarios at negligible cost.

These scenarios provide a comprehensive comparison framework. Scenario (i) illustrates the consequences of neglecting stabilization, Scenario (ii) represents the best achievable performance through experimental calibration, but restricted to fixed conditions, and Scenario (iii) demonstrates the effectiveness and flexibility of the proposed adaptive methodology, which maintains accuracy while ensuring generality and computational efficiency.

4 | Results and Discussion

The results presented in this section aim to demonstrate the accuracy, robustness, and efficiency of the proposed adaptive methodology for stabilizing engineering simulations. All codes were implemented in Python and executed on a Dell G15 laptop equipped with an Intel Core i5 (12th generation, up to 4.4 GHz), an NVIDIA GeForce RTX 3050 GPU, and 8 GB of DDR4–3200 MHz RAM. The simulations were executed in a standard CPU-based workflow; the GPU is reported for completeness, since it is part of the hardware environment. This specification ensures transparency in reproducibility and provides a practical baseline for assessing computational cost. An additional point of methodological rigor is that all simulations, including those carried out for the verification stage, were performed under the same physical and boundary conditions as the experiments described in Section 2. Such consistency is uncommon in the literature, where verification is often conducted under simplified setups, but it is a more rigorous procedure as it ensures that both verification and validation reflect the real operating conditions of the model.

The discussion is organized into six parts. First, the predictive equation linking the space–time grid parameters (N_y, N_t) to the optimal artificial viscosity factor is derived and evaluated, establishing the central element of the methodology. Next, the numerical implementation is verified through an apparent order of convergence analysis. Third, the methodology is validated against experimental grain-aeration data under identical operating conditions, comparing the proposed predictive law with both an unstabilized baseline and the conventional benchmark based on experimental calibration. Fourth, a sensitivity analysis is conducted to assess how the smoothness metric responds to variations in μ. Fifth, classical mesh refinement is examined as an alternative stabilization mechanism, quantifying the diminishing returns in oscillation attenuation relative to the rapidly increasing computational burden. Finally, computational cost is assessed using both wall-clock time and operation counts, highlighting that the predictive viscosity evaluation introduces negligible overhead while reproducing, on coarse grids, the stabilization effect that would otherwise require prohibitively fine resolutions.

4.1 | Derivation and Evaluation of the Predictive Equation

The core of the proposed methodology is the construction of a predictive relation between the grid parameters (N_y, N_t) and the optimal artificial viscosity factor μ_{opt}. This relation is obtained through polynomial regression applied to a dataset of optimal factors generated by systematic simulations. Although the case illustrated here corresponds to the aeration model discretized with the LS, the procedure is general and can be applied to any numerical formulation where AV is required.

To formalize the process, let us define a dataset

$$\mathcal{D} = \{(N_{y,i}, N_{t,i}, \mu_{\text{opt},i})\}_{i=1}^{M},$$

where each triplet corresponds to one simulation carried out with spatial resolution $N_{y,i}$, temporal resolution $N_{t,i}$, and the optimal viscosity factor $\mu_{\text{opt},i}$ determined for that grid.

The dataset $\mathcal{D}$ was constructed from a representative range of discretizations, with $N_y = \{30, 35, \ldots, 95, 100\}$ and $N_t = \{121, 241, 481, 721, 961, 1201\}$, resulting in a total of 90 distinct space–time grid configurations. For each configuration (N_y, N_t), the viscosity factor μ was systematically varied within the interval $[10^{-7}, 10^{-4}]$ using a fine increment of $\Delta\mu = 10^{-7}$, corresponding to one thousand candidate values per configuration. Altogether, this procedure required approximately 90,000 full simulations of the coupled heat and mass transfer equations, each evaluated with the smoothness metric to determine the optimal viscosity factor. The dense coverage of the parameter space ensures that the regression model is trained on a comprehensive dataset, capturing the dependency of μ on (N_y, N_t) in detail and avoiding heuristic approximations.

Using $\mathcal{D}$, polynomial regression models of increasing degree d were fitted to approximate the mapping

$$(N_y, N_t) \;\mapsto\; \mu_{\text{opt}},$$

resulting in the predictive law

$$\mu_{\text{Proposed}}(N_y, N_t) = \sum_{j+k\le d} c_{jk} N_y^j N_t^k,$$

with coefficients c_{jk} estimated via least squares. Polynomial degrees $d = 2, 4, 6, 8, 10$ were tested, allowing assessment of the trade-off between model complexity and predictive accuracy.

Figure 3 summarizes the results. The left panels compare the optimal viscosity factors μ_{opt} (black stars) with the values predicted by polynomial regressions of different orders. The right panels report the absolute errors $|\mu_{\text{opt}} - \mu_{\text{Proposed}}|$. Results are shown for three representative temporal resolutions: $N_t = 121$ (top), $N_t = 481$ (middle), and $N_t = 1201$ (bottom).

The results highlight several important points. For coarse temporal resolution ($N_t = 121$), low-order models such as $d = 2$ or $d = 4$ deviate significantly from the optimal factors, especially as N_y increases, leading to errors up to 10^{-5}. By contrast, higher-order models ($d = 6, 8, 10$) track the benchmark values much more closely, maintaining errors within the range 10^{-6}–10^{-5}. At intermediate resolution ($N_t = 481$), the same trend is observed: lower-order regressions struggle to capture the nonlinear variation of μ with N_y, while $d = 6$ and $d = 8$ exhibit excellent agreement across the entire range. Finally, at fine resolution ($N_t = 1201$), all models tend to converge, reflecting the smoother dependence of μ at higher N_t. In this case, even a fourth-order regression yields acceptable predictions, though higher-order models continue to offer the most accurate results.

Two conclusions emerge from this analysis. First, the predictive law generalizes the dependency of μ on (N_y, N_t), accurately capturing nonlinear behavior across the tested discretizations, particularly when $d = 6$ or $d = 8$ is used. Second, while including higher-order polynomial terms might appear to increase algorithmic complexity, the overhead is negligible compared with the dominant cost of solving the governing equations (shown later in Table 1). Therefore, for the remainder of this work, the sixth-order polynomial regression ($d = 6$) is adopted as the predictive law, since it provides a strong compromise between accuracy, robustness, and computational efficiency.

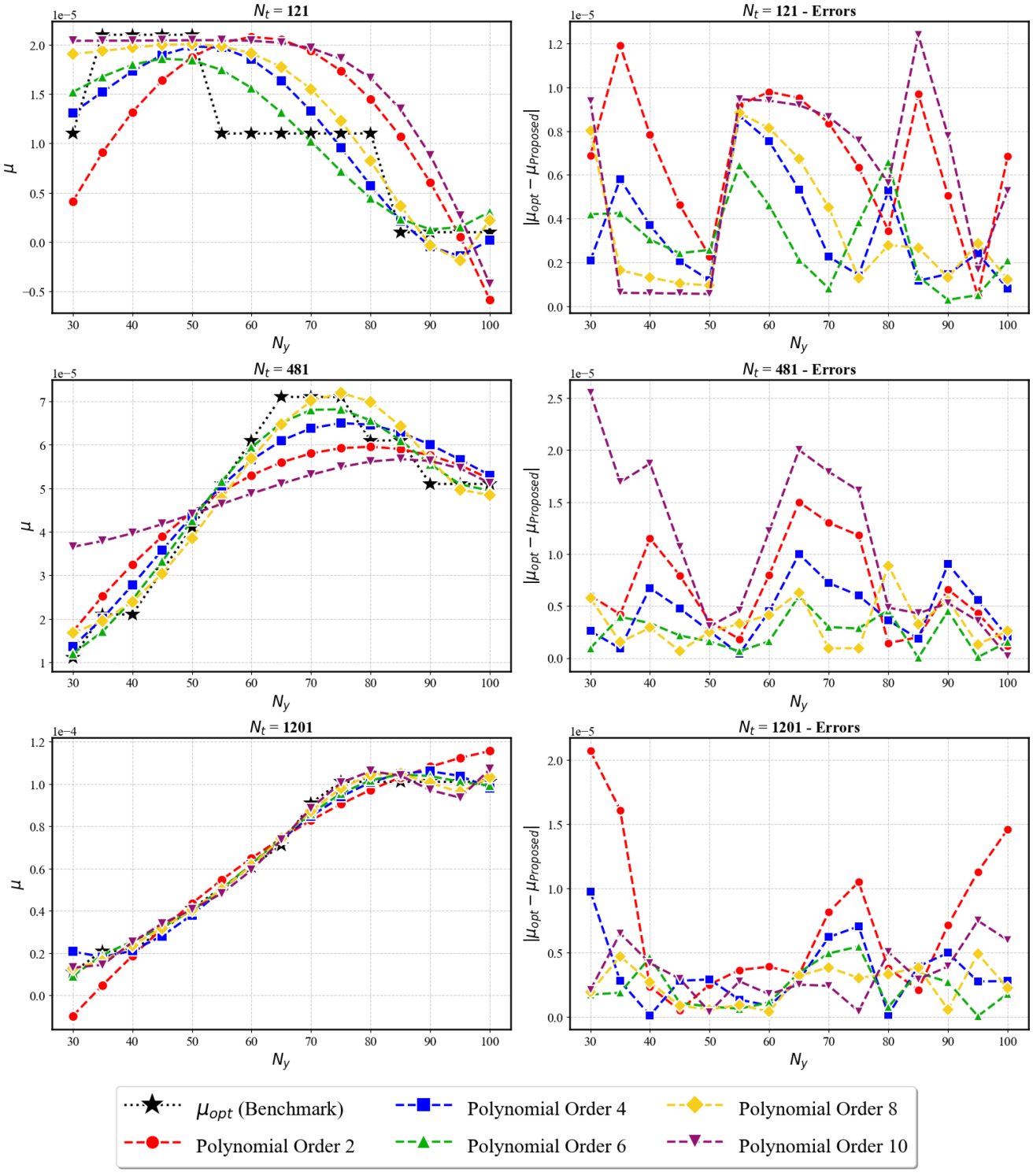

FIGURE 3 | Comparison between the optimal viscosity factor μ_{opt} (black stars) and the values predicted by polynomial regressions of order 2, 4, 6, 8, and 10 (left panels), along with their absolute errors (right panels), for three representative temporal resolutions $N_t = 121, 481, 1201$.

4.2 | Code Verification

The reliability of a numerical methodology depends not only on its agreement with experimental data but also on the internal consistency of its implementation. For this reason, before analyzing the aeration simulations, the proposed algorithm is subjected to a verification stage. Since no analytical solution exists for the coupled model, direct comparison with exact solutions is not possible. Instead, verification is conducted through an Apparent Order of Convergence (AOC) analysis,

TABLE 1 | Detailed breakdown of operations for different grid sizes, with and without the predictive viscosity law.

Grid (N_y, N_t)	Case	Additions	Multiplications	Divisions	Powers	Function calls
30×121	w/o μ_{Proposed}	118,110	258,240	131,940	44,910	220,073
	w/ μ_{Proposed}	118,136	258,294	131,940	44,937	220,080
60×241	w/o μ_{Proposed}	481,020	1,056,480	537,480	183,420	893,723
	w/ μ_{Proposed}	481,046	1,056,534	537,480	183,447	893,730
120×481	w/o μ_{Proposed}	1,941,240	4,272,960	2,169,360	741,240	3,601,823
	w/ μ_{Proposed}	1,941,266	4,273,014	2,169,360	741,267	3,601,830
240×961	w/o μ_{Proposed}	7,799,280	17,185,920	8,716,320	2,980,080	14,461,223
	w/ μ_{Proposed}	7,799,306	17,185,974	8,716,320	2,980,107	14,461,230
480×1921	w/o μ_{Proposed}	31,265,760	68,931,840	34,943,040	11,950,560	57,952,823
	w/ μ_{Proposed}	31,265,786	68,931,894	34,943,040	11,950,587	57,952,830

a well-established approach for problems where analytical benchmarks are unavailable but systematic mesh refinement can be performed [49].

The purpose of this step is twofold. First, it confirms that the discretization and implementation of the LS achieve the convergence behavior expected from the theoretical formulation. Second, it provides confidence that subsequent comparisons with experimental data reflect the physical assumptions of the model rather than coding or discretization errors. In this way, the verification stage establishes the foundation upon which the validation results are interpreted.

The AOC method estimates the effective convergence rate of the numerical solution as the grid is refined, offering a quantitative measure of numerical consistency. For three successively refined meshes with spatial resolutions $\Delta y_1 > \Delta y_2 > \Delta y_3$ and corresponding numerical solutions T_1, T_2, T_3, the apparent order p is given by [49, 50]

$$p = \frac{\ln\left(\frac{\|T_1 - T_2\|}{\|T_2 - T_3\|}\right)}{\ln(r)}, \tag{44}$$

where $\|\cdot\|$ denotes a chosen error norm (e.g., L_2 norm), and $r = \Delta y_1/\Delta y_2 = \Delta y_2/\Delta y_3$ is the constant refinement ratio. In practice, the L_2 norm over the entire spatial domain is adopted:

$$\|T_i - T_j\| = \sqrt{\frac{1}{N_y}\sum_{k=1}^{N_y}\left(T_i(y_k) - T_j(y_k)\right)^2}. \tag{45}$$

By construction, the numerical solution is expected to converge towards the theoretical order of accuracy of the LS, which is second order [29], as the mesh is sufficiently refined. In this study, convergence tests are performed by systematically refining both spatial and temporal discretizations, ensuring that the observed order reflects the combined effects of space–time resolution. To present the results clearly, a Grid Refinement Level (GRL) is defined, which serves as the abscissa in the convergence plots. Each GRL corresponds to one refinement step, obtained by doubling both the number of spatial nodes (N_y) and the number of time steps (N_t) relative to the preceding level. Thus, level 1 represents the baseline mesh ($N_y = 100$, $N_t = 300$), level 2 corresponds to ($N_y = 200$, $N_t = 600$), and so forth, with a uniform refinement ratio $r = 2$. For each level, a triplet of solutions (T_1, T_2, T_3) is generated to evaluate the apparent order p using Equation (44).

Figure 4 displays the spatial distribution of the AOC computed at selected points of the domain. The left panel shows the behavior of the proposed stabilized formulation, while the right panel presents the corresponding unstabilized case.

Remark. The convergence order reported in Figure 4 corresponds to a local apparent estimate, computed between successive mesh refinements, rather than to a global asymptotic rate. As such, it is inherently sensitive to transient effects, local variations in solution smoothness, and to the spatial and temporal activation of the artificial viscosity, which naturally explains the dispersion observed in the curves. The figure should therefore be interpreted as illustrating an asymptotic trend: the apparent order progressively approaches its limiting value as the mesh is refined, even though this limit is not

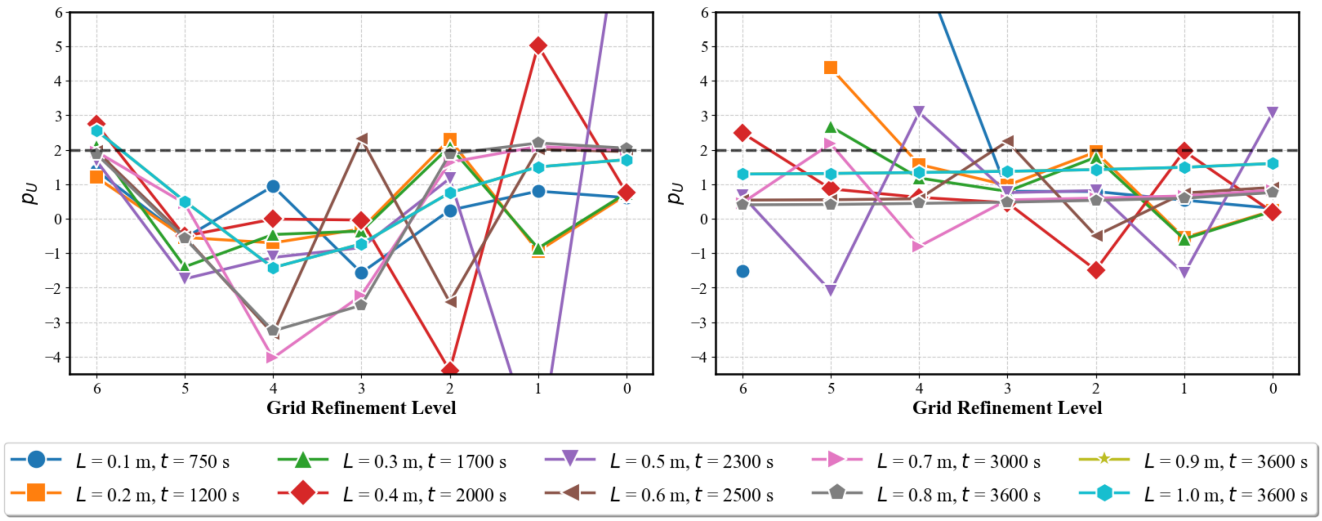

FIGURE 4 | Apparent order of convergence p at selected spatial and temporal points of the domain as a function of the *Grid Refinement Level* (GRL). Each GRL corresponds to a uniform doubling of both spatial and temporal resolution ($r = 2$). Left: results obtained with the proposed methodology, including artificial viscosity. Right: results without artificial viscosity.

fully attained within the range of resolutions considered. The asymptotic convergence regime only emerges at sufficiently fine resolutions; at moderate meshes, pre-asymptotic effects dominate. The mesh resolutions considered in this work are intentionally restricted to computationally feasible and experimentally relevant ranges, for which local fluctuations of the apparent order are expected and should not be misinterpreted as a lack of convergence.

It can be seen in Figure 4 that the proposed methodology (left panel) exhibits an AOC consistently approaching the theoretical second order, even at points characterized by steep temperature gradients. These locations correspond to the cooling front, where the grain temperature drops sharply due to aeration. Preserving accuracy in these regions is critical, as they govern the dynamics of the cooling process and thus the predictive capability of the model. In contrast, the results without AV (right panel) deviate substantially, with the estimated order often deteriorating or the simulation breaking down due to severe oscillations.

It is important to emphasize that the emergence of a second-order convergence trend should not be interpreted as an intrinsic improvement of the solution in regions with sharp gradients. In such regimes, locally first-order behavior is often expected once stabilization mechanisms become active. The role of the proposed methodology is not to enforce diffusion dominance, but to identify an optimal global stabilization level that suppresses spurious oscillations while avoiding excessive numerical diffusion. Unlike upwinding-based stabilization, where numerical diffusion is activated implicitly and locally, the proposed approach relies on an explicit and reproducible criterion to balance stability and accuracy.

While pointwise analyses of the apparent order provide valuable local insight, they can also be misleading, as numerical solutions often display spatial regions with distinct convergence behavior depending on local smoothness [49]. To provide a broader assessment of numerical consistency, Figure 5 presents the AOC as a function of the GRL for two representative indicators: (i) the apparent order evaluated at the mid-height of the grain column ($y = 0.5$ m) over the entire temporal evolution, capturing the local behavior in a region of strong gradients, and (ii) the global order obtained from the aggregated discretization error across the full spatiotemporal domain, reflecting the overall consistency of the solution.

Figure 5 indicates that the proposed methodology consistently recovers the theoretical second-order accuracy across all grid refinement levels. As the mesh is refined, both the local and global apparent orders converge steadily toward $p \approx 2$, confirming the numerical consistency of the stabilized formulation. In contrast, the unstabilized case exhibits irregular behavior.

To the best of the authors' knowledge, such a domain-wide AOC analysis has not previously been reported either for this specific model or for grain aeration simulations in general. By combining realistic initial conditions (drawn directly from the experimental dataset) with a domain-wide verification framework, this study provides a practical demonstration of

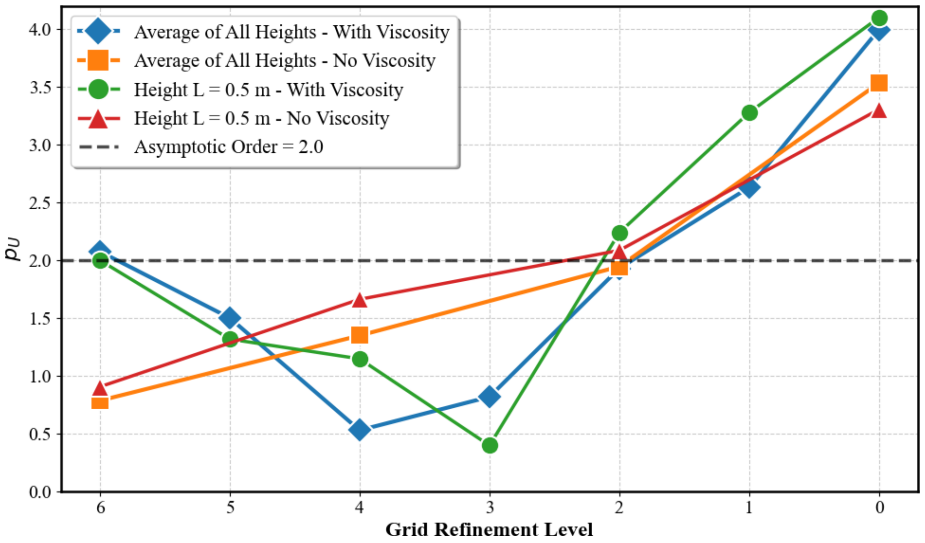

FIGURE 5 | Apparent order of convergence p as a function of the *Grid Refinement Level* (GRL). The solid line represents the order computed at the mid-height of the grain column ($y = 0.5$ m), and the dashed line indicates the global order obtained over the full spatiotemporal domain. Each GRL corresponds to a uniform doubling of both spatial and temporal resolutions ($r = 2$). The stabilized formulation consistently recovers second-order accuracy, whereas the unstabilized case shows significant degradation.

AOC analysis in this context. In contrast to the prevailing practice of assessing convergence on simplified or idealized setups, the present approach reflects the true conditions under which aeration models are intended to operate.

This dual verification strategy—encompassing pointwise, temporal, and domain-wide analyses—establishes a stringent assessment of numerical consistency. The findings demonstrate not only that the implementation is mathematically sound but also that it remains reliable under realistic operating conditions, thereby strengthening confidence in the subsequent validation and application stages.

4.3 | Validation With Experimental Data

After verifying the numerical implementation through AOC analysis, the next step is to assess whether the proposed methodology is able to reproduce real aeration experiments. Validation against experimental data is essential, as it establishes the practical relevance of the model and its ability to capture the physical behavior of grain cooling under realistic conditions.

By linking the viscosity factor μ directly to the discretization parameters (N_y, N_t) through the predictive equation, the method eliminates the need for repeated calibration and can be applied robustly to different scenarios. To demonstrate this advantage, the validation is carried out under three representative configurations: (i) no artificial viscosity, (ii) manual calibration using experimental data (benchmark), and (iii) the proposed predictive formulation.

To ensure a fair comparison, the parameters of all simulated cases are set equal to those of the experimental dataset (see Section 2.3). The validation is therefore performed under identical initial and boundary conditions, isolating the role of the AV treatment. Since the availability of experimental measurements is limited to a few sensor heights, the comparison is restricted to the corresponding locations, namely $y = 0.15, 0.27,\ 0.40,\ and\ 0.54\ m$. At each of these heights, the discrepancy between simulated and experimental temperature profiles is quantified using the mean absolute error (MAE). To obtain a single global indicator of accuracy across the entire set of heights, the mean squared error (MSE) is then computed over the MAE values:

$$\mathrm{MAE}(y) = \frac{1}{N_t}\sum_{n=1}^{N_t}\left|T^n_{\mathrm{sim}}(y) - T^n_{\mathrm{exp}}(y)\right|, \tag{46}$$

$$\mathrm{MSE} = \frac{1}{N_h}\sum_{j=1}^{N_h}\left(\mathrm{MAE}(y_j)\right)^2, \tag{47}$$

where N_t is the number of available experimental time steps at each height and N_h is the number of measurement heights.

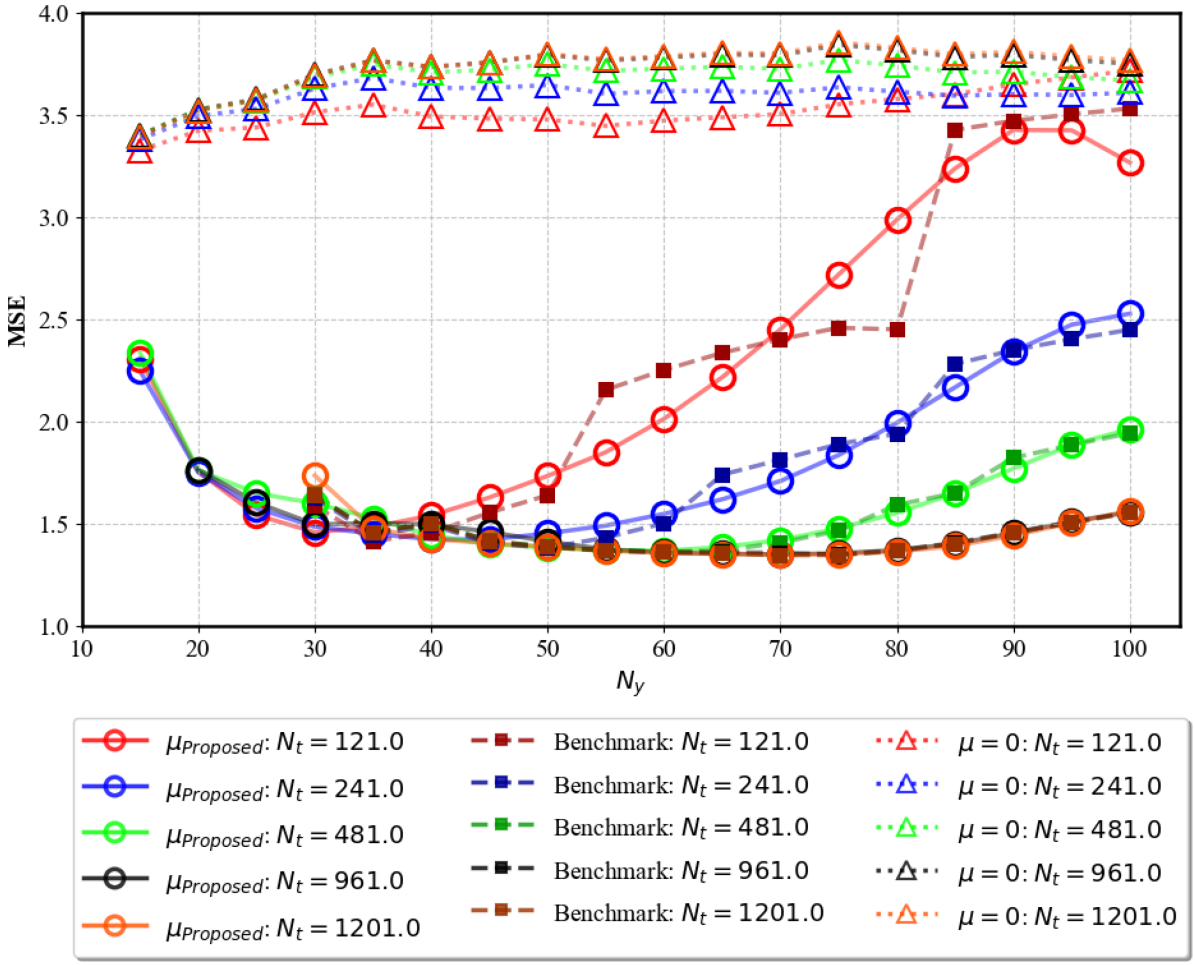

FIGURE 6 | Global mean squared error (MSE) between simulated and experimental data for various combinations of spatial and temporal discretization N_y, N_t.

This combined metric allows accuracy to be assessed both locally, at individual measurement positions, and globally, across the set of experimental observations. In this way, the evaluation not only accounts for the match at specific heights but also captures the overall predictive consistency of the numerical methodology.

Figure 6 summarizes the validation results by presenting the global mean squared error (MSE), defined in Equation (47), for different combinations of spatial and temporal resolutions (N_y, N_t). The figure includes results for the three test scenarios defined in Section 3.4: (i) the baseline case without artificial viscosity ($\mu = 0$), (ii) the conventional benchmark with viscosity manually calibrated against experimental measurements, and (iii) the proposed adaptive approach, where μ_{Proposed} is obtained directly from the grid parameters.

It can be seen in Figure 6 that the case without AV (dotted lines) consistently yields the highest errors, regardless of mesh resolution, confirming that oscillations dominate the solution when no stabilization is applied. The benchmark scenario (dashed lines) corresponds to the conventional approach in which the viscosity factor is tuned directly against experimental data. By construction, this strategy performs best, since μ is selected a posteriori to minimize the discrepancy between simulation and measurements.

Notably, the proposed adaptive methodology (solid lines) achieves errors that are virtually indistinguishable from those of the benchmark, despite not relying on experimental calibration. Instead, the factor $\mu_{\text{Proposed}}(N_y, N_t)$ is predicted solely from the discretization parameters. This demonstrates that the predictive law generalizes the stabilization process, delivering benchmark-level accuracy without the need for repeated calibration against experiments.

Another important observation from Figure 6 is that refining the temporal resolution from $N_t = 961$ to $N_t = 1201$ does not produce any noticeable improvement in accuracy. The error curves for these two grids essentially overlap, indicating

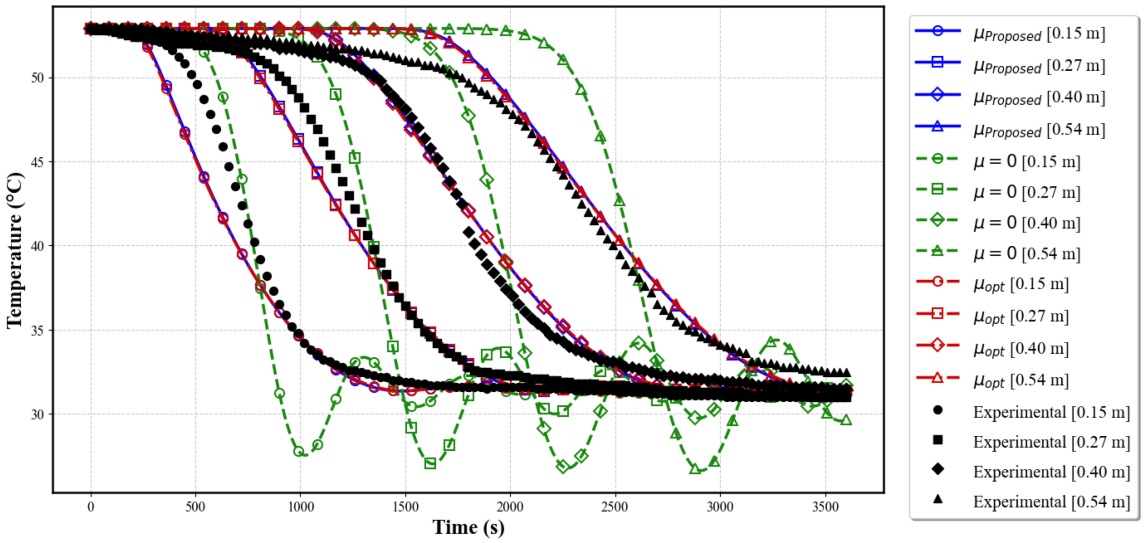

FIGURE 7 | Comparison between experimental temperature profiles and numerical simulations at four measurement heights (y = 0.15, 0.27, 0.40, and 0.54 m) for the grid configuration $N_y = 70$, $N_t = 1201$. Results are shown for the three numerical strategies: (i) no artificial viscosity ($\mu = 0$), (ii) manual calibration using experimental data (μ_{opt}), and (iii) the proposed predictive viscosity law (μ_{Proposed}).

that a practical resolution limit has been reached. Beyond this point, further refinement only increases computational cost without yielding tangible benefits.

This leads to a critical insight: once this plateau is reached, further mesh refinement increases computational cost without delivering meaningful gains in smoothness. Such saturation exposes the limitations of mesh-based stabilization and highlights the advantage of the proposed predictive methodology, which provides stable and accurate solutions directly from discretization parameters. By avoiding prohibitively fine grids and experiment-specific calibration, the predictive law enables reliable aeration simulations to be performed efficiently and consistently across different resolutions, thereby reinforcing both the generality and the predictive capability of the model.

Figure 7 presents a direct comparison between experimental temperature profiles and the three numerical strategies considered for the grid configuration $N_y = 70$ and $N_t = 1201$, which corresponds to the lowest error case identified in Figure 6.

It can be observed in Figure 7 that the simulation without artificial viscosity ($\mu = 0$) produces strongly oscillatory profiles, which deviate substantially from the experimental measurements. The manually calibrated case, by construction, provides the closest match to the experimental profiles, since μ is tuned specifically to minimize the discrepancy with the measured data.

The proposed methodology achieves results that are virtually indistinguishable from the manually calibrated benchmark. Despite not relying on any experimental input, the predictive viscosity law captures both the timing and magnitude of the cooling fronts across all measured heights, suppressing oscillations while preserving the physical dynamics of the process. Quantitatively, the MSE relative to experimental data reinforces this conclusion: the benchmark calibration yielded MSE = 1.342571, the unstabilized case yielded MSE = 3.799020, and the proposed predictive law yielded MSE = 1.345725. These values confirm that the predictive model reproduces benchmark-level accuracy.

The significance of this result lies in the fact that experimental calibration is inherently tied to specific conditions and cannot be generalized across different discretizations or scenarios. By contrast, the proposed methodology is transferable across discretizations: once the predictive coefficients are identified, the viscosity factor can be applied directly to any grid configuration, ensuring stability and accuracy at negligible cost. This reinforces the central contribution of the work: a robust and reproducible stabilization strategy that matches benchmark accuracy without experiment-dependent tuning.

TABLE 2 | Sensitivity of the smoothness metric and global mean squared error (MSE) with respect to the normalized artificial viscosity coefficient for $N_y = 70$ and $N_t = 1201$.

μ/μ_{opt}	$\sigma(\mu)$	MSE	μ/μ_{opt}	$\sigma(\mu)$	MSE
0.00	0.0	3.799020	1.15	9.895323×10^{-5}	1.343630
0.0025	1.344473×10^{-7}	3.739041	1.20	1.032555×10^{-4}	1.346056
0.05	2.688946×10^{-7}	3.683714	1.30	1.118601×10^{-4}	1.359477
0.10	5.377893×10^{-7}	3.585317	1.40	1.204648×10^{-4}	1.384732
0.20	1.720926×10^{-5}	2.166205	1.50	1.290694×10^{-4}	1.416841
0.40	3.441852×10^{-5}	1.756811	1.60	1.376740×10^{-4}	1.450344
0.60	5.162778×10^{-5}	1.541740	1.70	1.462787×10^{-4}	1.487443
0.80	6.883704×10^{-5}	1.403001	1.80	1.548833×10^{-4}	1.526451
1.00	8.604629×10^{-5}	1.345725	1.90	1.634879×10^{-4}	1.566892
1.10	9.465092×10^{-5}	1.342751	2.00	1.720925×10^{-4}	1.609800

4.4 | Sensitivity Analysis of the Smoothness Metric

Although the effectiveness of the proposed smoothness metric for automatically determining the artificial viscosity factor has been demonstrated in Section 4.3, it is also important to assess the sensitivity of the numerical results with respect to variations in the viscosity factor. Beyond identifying a single optimal value, this analysis aims to verify whether the proposed approach detects a robust operating range of AV, rather than a narrowly tuned or fragile optimum.

The sensitivity study is performed using the grid configuration $N_y = 70$ and $N_t = 1201$, which corresponds to the lowest global error identified in the validation analysis (Section 4.3). All physical parameters, initial and boundary conditions, are kept identical to the experimental validation case, ensuring that the influence of the artificial viscosity factor can be isolated and analyzed independently.

First, the optimal viscosity factor μ_{opt} is determined automatically using the proposed smoothness metric. Subsequently, additional simulations are carried out by systematically varying the viscosity factor from the unstabilized case ($\mu = 0$) to values significantly larger than the automatically selected reference. This procedure allows the numerical behavior to be examined both in under- and over-stabilized regimes. For each simulation, the smoothness metric $\sigma(\mu)$ and the global mean squared error (MSE), defined in Equation (47), are evaluated. The numerical results are summarized in Table 2.

The results reveal a clear and physically consistent trend. In the absence of AV ($\mu = 0$), the numerical solution exhibits the largest MSE, indicating pronounced numerical oscillations and poor agreement with experimental data. As the viscosity factor is increased from zero, the MSE decreases rapidly, reflecting the effective suppression of nonphysical oscillations.

Importantly, the minimum error is not attained at a single isolated value of μ, but rather within an interval around μ_{opt}. Within this range, variations in the viscosity coefficient led to only marginal changes in the MSE, indicating that the proposed method identifies a stable and robust operating regime rather than a narrowly tuned optimal point.

Beyond this interval, further increases in μ result in a gradual deterioration of accuracy due to excessive numerical diffusion, which progressively damps physically relevant gradients. This behavior is consistently reflected by the smoothness metric $\sigma(\mu)$, which increases monotonically with μ as the stabilization strength grows and local variations are increasingly penalized.

Additionally, it is worth noting that the number of simulations used to assemble the regression dataset (approximately 90,000) is mainly a consequence of adopting an extremely fine sweep in viscosity, $\Delta\mu = 10^{-7}$, over the wide interval $[10^{-7}, 10^{-4}]$. The sensitivity results in Table 2 indicate, however, that the minimum error is not confined to a sharply tuned value: the MSE remains essentially flat over a broad neighborhood of μ_{opt}. In particular, the MSE stays within approximately 1.3% of its minimum value for $\mu/\mu_{\text{opt}} \in [1.0,\ 1.3]$ (from 1.345725 at $\mu/\mu_{\text{opt}} = 1.0$ to 1.359477 at $\mu/\mu_{\text{opt}} = 1.3$, with the minimum 1.342751 at $\mu/\mu_{\text{opt}} = 1.1$).

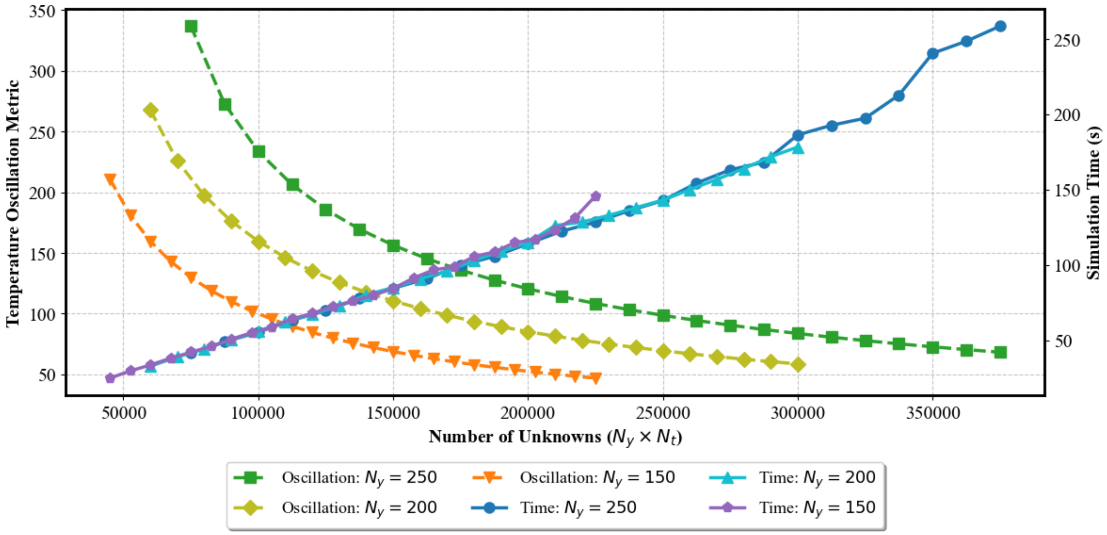

FIGURE 8 | Temperature oscillation metric and simulation runtime as a function of the total number of unknowns ($N_y \times N_t$), for different spatial resolutions.

This observation suggests that the construction of $\mathcal{D}$ does not require an exhaustive search over the full interval with such a small increment. For instance, the sweep could be restricted to the practically optimal band $\mu \in [\ 1.0\ \mu_{\text{opt}},\ 1.3\ \mu_{\text{opt}}\ ], \Delta\mu = 0.01\ \mu_{\text{opt}}$, which would require only 31 candidate values per grid configuration (instead of 1000). For the 90 space-time grids used here, this would reduce the total cost from about 90,000 to $90 \times 31 = 2790$ simulations, that is, a reduction of approximately 96.9% in the dataset-generation effort, while still targeting the same robust operating regime identified by the sensitivity study.

It should be emphasized, however, that this potential reduction is discussed only as a post-analysis insight enabled by the sensitivity study. At the stage of constructing $\mathcal{D}$, the location and width of the robust operating band around μ_{opt} are not known *a priori*, and therefore restricting the search interval cannot be assumed as part of the general procedure. Accordingly, the reduced sweep is not adopted here: all remaining results reported in this paper are obtained using the original wide interval $[10^{-7}, 10^{-4}]$ with $\Delta\mu = 10^{-7}$, ensuring that μ_{opt} is identified without relying on any precondition.

4.5 | Mesh Refinement as a Stabilization Mechanism

As mentioned, mesh refinement is a well-established strategy for reducing numerical oscillations in engineering problems. By increasing spatial and temporal resolution, dispersive errors associated with the discrete advective operator are progressively attenuated, and the numerical solution converges toward a smoother regime. In this subsection, the effectiveness and limitations of mesh refinement are assessed quantitatively using the smoothness metric introduced in Section 3.3.2.

Figure 8 summarizes the refinement study by reporting the temperature oscillation metric as a function of the total number of unknowns, $N_y \times N_t$, for different spatial resolutions. In addition to the smoothness indicator, Figure 8 also reports the corresponding wall-clock runtime of each simulation, allowing the reduction of oscillations achieved by refinement to be interpreted directly against its computational cost.

As expected, mesh refinement leads to a systematic reduction of numerical oscillations: coarse grids exhibit pronounced oscillatory behavior, while successive refinements progressively smooth the solution. However, Figure 8 also reveals an important limitation of refinement-based stabilization. Although oscillations decrease monotonically with increasing resolution, the rate of reduction diminishes rapidly as the mesh is refined. Beyond a moderate number of unknowns, additional refinement produces only marginal improvements in smoothness, indicating an asymptotic saturation of the refinement effect. In other words, increasingly fine meshes yield progressively smaller reductions in oscillation intensity.

This diminishing return contrasts sharply with the associated computational cost. As shown in Figure 8, the simulation time increases nearly linearly with the number of unknowns, while the oscillation metric decreases at a much slower rate.

TABLE 3 | Computational effort required to reach the target smoothness level $\sigma^\star$ using mesh refinement without artificial viscosity. The oscillation metric σ is reported for the three prognostic variables.

Grid (N_y, N_t)	Simulation time [s]	σ_T	σ_U	σ_R	Meets criterion?
50×121	3.098538	127.048615	0.003233	0.001221	No
100×241	12.581981	113.222023	0.002704	0.000995	No
150×481	37.961669	80.254614	0.001750	0.000636	No
200×721	76.697670	67.748234	0.001416	0.000511	No
250×1201	162.129754	49.845526	0.000972	0.000348	Yes

Consequently, the computational effort grows disproportionately relative to the numerical benefit obtained. Achieving a modest additional reduction in oscillations requires a substantial increase in resolution and execution time.

As a result, oscillation levels comparable to those obtained with the proposed artificial viscosity formulation are reached only at very fine resolutions, involving several hundred thousand degrees of freedom. This demonstrates that, although mesh refinement can indeed suppress numerical oscillations, it rapidly becomes an inefficient stabilization strategy for engineering problems such as grain aeration.

4.6 | Computational Cost

Beyond accuracy and stability, the practical applicability of a numerical methodology depends critically on computational efficiency. In grain aeration modeling, simulations are often carried out repeatedly in parametric studies or optimization workflows, where the computational burden can quickly become prohibitive. It is therefore essential to assess not only the accuracy of the proposed algorithm, but also its cost relative to refinement-based stabilization.

The previous section showed that mesh refinement can reduce numerical oscillations, albeit with progressively smaller gains as resolution increases. Here, the corresponding cost question is addressed: what is the computational price of reaching a prescribed smoothness level by refinement alone?

To compare both strategies on equal footing, a baseline discretization (N_y, N_t) is fixed and a target smoothness level $\sigma^\star$ is defined as the global smoothness (Equation 36) achieved by the proposed viscosity law on that grid:

$$\sigma^\star \equiv \sigma\left(\mu_{\text{Proposed}}; N_y, N_t\right).$$

In the baseline case with $N_y = 50$ and $N_t = 121$, the full optimization of the proposed methodology required 39.8 s. It is important to note that this corresponds to the one-time training stage of the algorithm, performed only once during the first execution. After this step, the predictive law provides the optimal viscosity factor directly, reducing the execution time of subsequent simulations to only 3.49 s. For the baseline configuration, the oscillation metric yielded

$$\sigma^\star = 51.890838,$$

with $\mu_{\text{Proposed}} = 2.1 \times 10^{-5}$, which serves as the benchmark for comparison.

To reach the same smoothness level without AV, a series of simulations was performed with progressively refined grids. Table 3 summarizes the required computational effort and the oscillation metrics for the three prognostic variables. The last column, "Meets criterion?", indicates whether the simulation achieved the target smoothness threshold $\sigma^\star = 51.89$ for the temperature field. A "Yes" entry denotes that the corresponding grid refinement successfully reduced σ_T below this reference level, whereas "No" entries represent cases where residual oscillations persisted above the threshold.

From Table 3, it becomes evident that oscillations arise exclusively in the temperature field, with σ_T values starting at 127.048615 for the baseline grid $(50, 121)$ and only falling below the target $\sigma^\star = 51.89$ at the refined grid $(250, 1201)$, where $\sigma_T = 49.845526$. By contrast, both moisture (σ_U) and humidity ratio (σ_R) remain consistently smooth across all refinements, never exceeding $\mathcal{O}(10^{-3})$. This selective behavior confirms that the proposed methodology intervenes only where necessary, damping spurious oscillations in the energy equation while preserving the physical fidelity of the mass

balance equations. A detailed diagnostic analysis of the numerical mechanism responsible for the onset of temperature oscillations is provided in Appendix B. The appendix traces the oscillatory behavior to the discrete advective operator in the energy balance equation and to its transient activation during the passage of sharp thermal fronts.

The computational implications of achieving $\sigma^\star$ via mesh refinement are striking: the simulation time grows from 3.098538 s in the baseline case to 162.129754 s for the refined grid, a 52-fold increase. And yet, all of this extra effort merely recovers the same level of smoothness that the predictive viscosity law delivers directly on the baseline grid. In other words, what refinement accomplishes at the cost of more than two orders of magnitude in additional operations, the proposed methodology achieves immediately, with negligible overhead.

To complement wall-clock timings, the computational complexity was also analyzed in terms of floating-point operations. This architecture-independent measure further illustrates that the predictive viscosity law adds virtually no overhead. Table 1 presents a breakdown of operation counts across different grid sizes, comparing simulations without (w/o μ_{Proposed}) and with (w/μ_{Proposed}) the predictive artificial viscosity law. The negligible differences between these pairs confirm that the stabilization introduces only a few additional arithmetic operations per time step, leaving the overall computational cost virtually unchanged.

Table 1 shows that the inclusion of the predictive law increases the operation count by only 129 operations, regardless of grid size. This fixed increment is computationally negligible when compared to the tens or hundreds of millions of operations required to solve the governing equations. In percentage terms, the overhead remains below 0.01% even for the smallest grid. Thus, the complexity of the physical problem vastly exceeds that of the stabilization procedure, ensuring that the predictive law preserves computational efficiency while guaranteeing stability.

In summary, the proposed methodology achieves the same or better smoothness than conventional mesh refinement at a fraction of the computational cost. Its overhead is negligible both in terms of wall-clock time and operation counts, while its selective action ensures that only the necessary variable (temperature) is stabilized. This makes the method particularly attractive for large-scale or parametric studies, where computational savings directly translate into practical feasibility.

5 | Conclusions

This study introduced a predictive framework to mitigate numerical oscillations in advection-dominated problems by reformulating artificial viscosity as a parameter inferred directly from discretization settings, rather than obtained through empirical tuning. A smoothness metric was developed to quantify spurious oscillations, enabling an offline optimization stage that produced a closed-form predictive law via polynomial regression. The approach was implemented in a one-dimensional, transient, and coupled heat-moisture transport model discretized by finite differences using the Leith scheme. Grain aeration was deliberately selected as a demanding case study with available experimental data, providing a stringent validation setting while maintaining relevance for realistic engineering simulations.

Verification based on apparent-order-of-convergence analysis confirmed recovery of second-order accuracy across the full spatiotemporal domain, including regions with steep gradients, whereas the unstabilized formulation exhibited significant order degradation and irregular behavior. Validation against experimental temperature measurements demonstrated that the predictive law reproduced observed profiles with accuracy essentially equivalent to manual calibration (MSE = 1.3457 *vs*. 1.3426), while eliminating the need for parameter sweeps. From a computational standpoint, the proposed workflow achieved the target smoothness level with an offline cost of 39.8 s, substantially below the 162.1 s required by refinement-only stabilization, while subsequent simulations required only 3.5 s and incurred negligible overhead. Notably, oscillations were confined to the temperature field, whereas moisture and humidity-related quantities remained naturally smooth across all tested grids, indicating that stabilization is effectively selective and primarily needed in the discrete energy balance.

A practical advantage of the framework is that the additional computational burden is incurred exclusively during the initial offline optimization stage, performed once for a given solver configuration and representative operating setup. After this one-time stage, the viscosity coefficient can be evaluated directly from (N_y, N_t) and reused across subsequent runs, whose cost is comparable to that of a conventional stabilized simulation. This amortization makes the approach particularly attractive for parametric studies, sensitivity analyses, and design-oriented simulation campaigns, where repeated executions are unavoidable and traditional tuning strategies would require recurrent calibration effort.

The main contributions of this work are: (i) formulation of a robust smoothness metric that autonomously identifies the artificial viscosity coefficient; (ii) derivation of a closed predictive law $\mu(N_y, N_t)$ that eliminates empirical calibration while preserving the expected convergence behavior; (iii) demonstration of stable, smooth, and efficient simulations with a one-time optimization cost and negligible overhead in subsequent runs; (iv) implementation of a global apparent-order-of-convergence verification procedure, providing a reproducible benchmark for coupled nonlinear transport models under realistic operating conditions; (v) evidence, for the grain-aeration model studied, that stabilization is required primarily in the energy balance, while the moisture and humidity dynamics remain intrinsically well-behaved.

Overall, the proposed predictive framework provides a general, efficient, and reproducible stabilization strategy for coupled transport simulations. By decoupling numerical stabilization from empirical calibration and amortizing the optimization cost across multiple simulations, the methodology extends beyond grain aeration to a broad range of engineering applications affected by spurious numerical oscillations.

Funding

This study was financed in part by the Coordenação de Aperfeiçoamento de Pessoal de Nível Superior – Brasil (CAPES) – Finance Code 001.

Conflicts of Interest

The authors declare no conflicts of interest.

Data Availability Statement

The data that support the findings of this study are available from the corresponding author upon reasonable request.

References

1. T. Shilt, P. J. O'Hara, and J. J. McNamara, "Stabilization of Advection Dominated Problems Through a Generalized Finite Element Method," *Computer Methods in Applied Mechanics and Engineering* 383 (2021): 113889, https://doi.org/10.1016/j.cma.2021.113889.

2. S. Wang and G. Yuan, "Discrete Strong Extremum Principles for Finite Element Solutions of Advection-Diffusion Problems With Nonlinear Corrections," *International Journal for Numerical Methods in Fluids* 96, no. 12 (2024): 1990–2005, https://doi.org/10.1002/fld.5330.

3. A. Kashefi, "Coarse Grid Projection Methodology: A Partial Mesh Refinement Tool for Incompressible Flow Simulations," *Bulletin of the Iranian Mathematical Society* 46, no. 1 (2020): 177–181, https://doi.org/10.1007/s41980-019-00249-9.

4. Z. Wu and Y.-X. Ren, "A Shock Capturing Artificial Viscosity Scheme Consistent With the Compact High-Order Finite Volume Methods," *Journal of Computational Physics* 516 (2024): 113291, https://doi.org/10.1016/j.jcp.2024.113291.

5. A. Prakash and Y. J. Zhang, "Projection-Based Reduced Order Modeling and Data-Driven Artificial Viscosity Closures for Incompressible Fluid Flows," *Journal of Computational Physics* 514 (2024): 113304, https://doi.org/10.1016/j.jcp.2024.113304.

6. J. Dickenson, J. M. Buick, J. Radulovic, and J. Bull, "Challenges in Cfd Model Validation: A Case Study Approach Using Ansys Cfx and Turbogrid," *Machines* 13, no. 7 (2025): 593, https://doi.org/10.3390/machines13070593.

7. F. F. Grinstein, L. G. Margolin, and W. J. Rider, *Implicit Large Eddy Simulation* (Cambridge University Press, 2007).

8. R. J. LeVeque, *Finite Volume Methods for Hyperbolic Problems*. Cambridge Texts in Applied Mathematics (Cambridge University Press, 2002).

9. P. Madhukar, L. M. Pandey, and U. S. Dixit, "Post-Harvest Grain Storage: Methods, Factors, and Eco-Friendly Solutions," *Food Control* 174 (2025): 111236, https://doi.org/10.1016/j.foodcont.2025.111236.

10. G. R. Thorpe, "Ch. 4 Physical Basics of Aeration," in *The Mechanics and Physics of Modern Grain Aeration Management* (CRC Press, 2001), 125–185.

11. D. C. Lopes, J. H. Martins, E. C. Melo, and P. M. B. Monteiro, "Aeration Simulation of Stored Grain Under Variable Air Ambient Conditions," *Postharvest Biology and Technology* 42, no. 1 (2006): 115–120, https://doi.org/10.1016/j.postharvbio.2006.05.007.

12. D. C. Lopes, A. J. Steidle Neto, and J. K. Santiago, "Comparison of Equilibrium and Logarithmic Models for Grain Drying," *Biosystems Engineering* 118 (2014): 105–114, https://doi.org/10.1016/j.biosystemseng.2013.11.011.

13. D. C. Lopes, A. J. Steidle Neto, and R. Vasco, Jr., "Comparison of Equilibrium Models for Grain Aeration," *Journal of Stored Products Research* 60 (2015): 11–18, https://doi.org/10.1016/j.jspr.2014.11.001.

14. D. Rigoni, M. A. V. Pinto, and J. E. Kwiatkowski, Jr., "Verification and Error Analysis for the Simulation of the Grain Mass Aeration Process Using the Method of Manufactured Solutions," *Biosystems Engineering* 223 (2022): 149–160, https://doi.org/10.1016/j.biosystemseng.2022.08.006.

15. D. Rigoni, M. A. V. Pinto, and J. E. Kwiatkowski, Jr., "On Space–Time Ratio in the Soybean Mass Aeration Problem Using a Manufactured Solution With Realistic Parameters," *Computers and Electronics in Agriculture* 214 (2023): 108300, https://doi.org/10.1016/j.compag.2023.108300.

16. C. E. Leith, "Numerical Simulation of the Earth's Atmosphere," *Methods in Computational Physics* 4 (1965): 1–28.

17. O. A. Khatchatourian and F. A. Oliveira, "Mathematical Modeling of Airflow and Thermal State in Large Aerated Grain Storage," *Biosystems Engineering* 95, no. 2 (2006): 159–169, https://doi.org/10.1016/j.biosystemseng.2006.05.009.

18. W. L. Oberkampf and T. G. Trucano, "Verification and Validation in Computational Fluid Dynamics," *Progress in Aerospace Sciences* 38, no. 3 (2002): 209–272, https://doi.org/10.1016/S0376-0421(02)00005-2.

19. B. Lecampion, A. Bunger, and X. Zhang, "Numerical Methods for Hydraulic Fracture Propagation: A Review of Recent Trends," *Journal of Natural Gas Science and Engineering* 49 (2018): 66–83, https://doi.org/10.1016/j.jngse.2017.10.012.

20. S. A. Lima, K. Mayeda, and M. Kamrujjaman, "Advanced Solutions of Nonlinear Convection–Diffusion–Reaction Equations Using the Finite Element Method," *Nonlinear Analysis: Modelling and Control* 4 (2025): 100047, https://doi.org/10.1016/j.nls.2025.100047.

21. A. Borg, B. Paulsen Husted, and O. Njå, "The Concept of Validation of Numerical Models for Consequence Analysis," *Reliability Engineering & System Safety* 125 (2014): 36–45, https://doi.org/10.1016/j.ress.2013.09.009.

22. A. S. White and R. Sinclair, "Quantitative validation techniques: a database. (i). simple examples," *Simulation Modelling Practice and Theory* 12, no. 6 (2004): 451–473, https://doi.org/10.1016/j.simpat.2004.06.001.

23. G. R. Thorpe, "Ch. 3 Ambient Air Properties in Aeration," in *The Mechanics and Physics of Modern Grain Aeration Management* (CRC Press, 2001), 79–120.

24. A. J. Hunter, "An Isostere Equation for Some Common Seeds," *Journal of Agricultural Engineering Research* 37, no. 3–4 (1987): 93–105, https://doi.org/10.1016/S0021-8634(87)80008-2.

25. D. Chung and H. Pfost, "Adsorption and Desorption of Water Vapor by Cereal Grains and Their Products Part i: Heat and Free Energy Changes of Adsorption and Desorption," *Transactions of the ASABE* 10 (1967): 549–551, https://doi.org/10.13031/2013.39726.

26. M. Benkhaled, S.-E. Ouldboukhitine, A. Bakkour, and S. Amziane, "A 1d Model for Predicting Heat and Moisture Transfer Through a Hemp-Concrete Wall Using the Finite-Element Method," *Materials* 14, no. 22 (2021): 6903, https://doi.org/10.3390/ma14226903.

27. S. S. Panigrahi, C. B. Singh, and J. Fielke, "A 3d Transient Cfd Model to Predict Heat and Moisture Transfer in On-Farm Stored Grain Silo Through Parallel Computing Using Compiler Directives: Impact of Discretization Methods on Solution Efficacy," *Drying Technology* 41, no. 7 (2023): 1133–1147, https://doi.org/10.1080/07373937.2022.2121284.

28. J. C. Tannehill and D. A. Anderson, *Computational Fluid Mechanics and Heat Transfer*, 2nd ed. (Taylor & Francis, 1997).

29. M. Dehghan, "Quasi-Implicit and Two-Level Explicit Finite-Difference Procedures for Solving the One-Dimensional Advection Equation," *Applied Mathematics and Computation* 167, no. 1 (2005): 46–67, https://doi.org/10.1016/j.amc.2004.06.067.

30. B. Bastl, M. Brandner, K. Slabá, and E. Turnerová, "Consistent Streamline Residual-Based Artificial Viscosity Stabilization for Numerical Simulation of Incompressible Turbulent Flow by Isogeometric Analysis," *Applications of Mathematics* 67, no. 6 (2022): 805–829, https://doi.org/10.21136/AM.2022.0131-21.

31. F. Denner, F. Evrard, R. Serfaty, and B. G. M. van Wachem, "Artificial Viscosity Model to Mitigate Numerical Artefacts at Fluid Interfaces With Surface Tension," *Computers & Fluids* 143 (2017): 59–72, https://doi.org/10.1016/j.compfluid.2016.11.006.

32. J. von Neumann and R. D. Richtmyer, "A Method for the Numerical Calculation of Hydrodynamic Shocks," *Journal of Applied Physics* 21, no. 3 (1950): 232–237, https://doi.org/10.1063/1.1699639.

33. V. Zingan, J.-L. Guermond, J. Morel, and B. Popov, "Implementation of the Entropy Viscosity Method With the Discontinuous Galerkin Method," *Computer Methods in Applied Mechanics and Engineering* 253 (2013): 479–490, https://doi.org/10.1016/j.cma.2012.08.018.

34. M.-C. Yue, X.-H. Wang, Z.-F. Liu, et al., "Application of Adaptive Artificial Viscosity Method to Reduce Grid Orientation Effect in Numerical Simulations for Steam Thermal Recovery," *Arabian Journal for Science and Engineering* 50 (2025): 10359–10384, https://doi.org/10.1007/s13369-024-09865-y.

35. M. Caldana, P. F. Antonietti, and L. Dede', "Discovering Artificial Viscosity Models for Discontinuous Galerkin Approximation of Conservation Laws Using Physics-Informed Machine Learning," *Journal of Computational Physics* 520 (2025): 113476, https://doi.org/10.1016/j.jcp.2024.113476.

36. A. H. S. Moghadam, E. Schillaci, and G. Alfonsi, "On the Evaluation of Mesh Resolution for Large-Eddy Simulation," *Fluids* 6, no. 1 (2021): 24, https://doi.org/10.3390/fluids6010024.

37. R. Tominec and M. Nazarov, "Residual Viscosity Stabilized Rbf-Fd Methods for Solving Nonlinear Conservation Laws," *Journal of Scientific Computing* 94, no. 1 (2023): 21, https://doi.org/10.1007/s10915-022-02055-8.

38. G. Vivarelli, N. Qin, and S. Shahpar, "A Review of Mesh Adaptation Technology Applied to Computational Fluid Dynamics," *Fluids* 10, no. 5 (2025): 129, https://doi.org/10.3390/fluids10050129.

39. A. Schwarz, D. Kempf, J. Keim, P. Kopper, C. Rohde, and A. Beck, "Comparison of Entropy Stable Collocation High-Order Dg Methods for Compressible Turbulent Flows," *Computers & Fluids* 303 (2025): 106874, https://doi.org/10.1016/j.compfluid.2025.106874.

40. A. Harten, "High Resolution Schemes for Hyperbolic Conservation Laws," *Journal of Computational Physics* 49, no. 3 (1983): 357–393, https://doi.org/10.1016/0021-9991(83)90136-5.

41. P. K. Sweby, "High Resolution Schemes Using Flux Limiters for Hyperbolic Conservation Laws," *SIAM Journal on Numerical Analysis* 21, no. 5 (1984): 995–1011, https://doi.org/10.1137/0721062.

42. G. E. Barter and D. L. Darmofal, "Shock Capturing With Pde-Based Artificial Viscosity for Dgfem: Part I. Formulation," *Journal of Computational Physics* 229, no. 5 (2010): 1810–1827, https://doi.org/10.1016/j.jcp.2009.11.010.

43. A. Klöckner, T. Warburton, and J. S. Hesthaven, "Viscous Shock Capturing in a Time-Explicit Discontinuous Galerkin Method," *Mathematical Modelling of Natural Phenomena* 6, no. 3 (2011): 57–83, https://doi.org/10.1051/mmnp/20116303.

44. J.-L. Guermond, R. Pasquetti, and B. Popov, "Entropy Viscosity Method for Nonlinear Conservation Laws," *Journal of Computational Physics* 230, no. 11 (2011): 4248–4267, https://doi.org/10.1016/j.jcp.2010.11.043.

45. P.-O. Persson and J. Peraire, "Sub-Cell Shock Capturing for Discontinuous Galerkin Methods," in *Proceedings of the 44th AIAA Aerospace Sciences Meeting and Exhibit* (American Institute of Aeronautics and Astronautics (AIAA), 2006), 112.

46. G. E. Karniadakis and S. J. Sherwin, *Spectral/Hp Element Methods for Computational Fluid Dynamics*, 2nd ed. (Oxford University Press, 2005).

47. S. K. Lele, "Compact Finite Difference Schemes With Spectral-Like Resolution," *Journal of Computational Physics* 103, no. 1 (1992): 16–42, https://doi.org/10.1016/0021-9991(92)90324-R.

48. S. B. Pope, *Turbulent Flows* (Cambridge University Press, 2000).

49. P. J. Roache, *Fundamentals of Computational Fluid Dynamics* (Hermosa Publishers, 1998).

50. P. D. Zen, M. Pinto, and S. R. Franco, "A Multigrid Waveform Relaxation Method for Solving the Nonlinear Silicon Problem With Relaxing Boundary Conditions," *Numerical Heat Transfer, Part B: Fundamentals* 86, no. 3 (2024): 3002–3018, https://doi.org/10.1080/10407790.2024.2351543.

51. D. B. Brooker, F. W. Barker-Arkema, and C. W. Hall, *Drying and Storage of Grains and Oilseeds* (AVI Book Van Nostrand Reinhold, 1992).

52. D. S. Jayas and S. Cenkowski, "Ch. 24 Grain Property Values and Their Measurement," in *Handbook of Industrial Drying* (CRC Press, 2006).

53. F. Fleurat-Lessard, "Qualitative Reasoning and Integrated Management of the Quality of Stored Grain: A Promising New Approach," *Journal of Stored Products Research* 38, no. 3 (2002): 191–218, https://doi.org/10.1016/S0022-474X(01)00022-4.

Appendix A

Definition of Symbols

This appendix gathers, in a single place, the notation adopted throughout the manuscript. Its purpose is to improve readability and to ensure that the governing equations, initial and boundary conditions, and numerical algorithm can be reproduced without ambiguity. In particular, the aeration model combines thermophysical parameters, psychrometric relations, and numerical quantities introduced at different stages of the presentation; the tables below provide a consistent reference for symbols, physical meaning, and units.

All quantities are reported in SI units. Temperature is expressed in °C; since the model involves temperature *increments* in derivatives and fluxes, °C and K are equivalent for dimensional purposes. Dimensionless parameters used for stabilization and diagnostics (e.g., Courant number, artificial-viscosity factor, and smoothness metric) are listed explicitly to distinguish numerical control variables from physical properties.

Definition of Symbols and Units

Table A1 summarizes the physical and model parameters, while Table A2 lists the numerical and discretization parameters. Together, they define the complete notation employed in Sections 2–4.

TABLE A1 | Physical and model parameters: Definition, physical meaning, and units.

Symbol	Physical meaning	Definition/description	Unit
t	Time	Independent temporal variable	s
y	Vertical coordinate	Spatial coordinate along airflow direction	m
L	Silo height	Vertical extent of the computational domain	m
T	Grain temperature	Average grain temperature	°C
U	Grain moisture (dry basis)	Ratio of water mass to dry matter mass	kg kg^{-1}
R	Humidity ratio	Mass of water vapor per mass of dry air	kg kg^{-1}
u_a	Air velocity	Superficial velocity of aeration airflow	m s^{-1}
ρ_a	Air density	Density of intergranular air	kg m^{-3}
ρ_σ	Bulk grain density	Apparent density of grain bulk	kg m^{-3}
ε	Porosity	Fraction of void volume in the grain bulk	—
c_g	Grain specific heat	Heat capacity of dry grain	Jkg^{-1} °C^{-1}
c_W	Water specific heat	Heat capacity of liquid water	Jkg^{-1} °C^{-1}
c_a	Air specific heat	Heat capacity of dry air	Jkg^{-1} °C^{-1}
h_v	Latent heat of vaporization	Energy required to vaporize water	J kg^{-1}
h_s	Differential heat of sorption	Energy associated with moisture sorption	J kg^{-1}
$\frac{dm}{dt}$	Dry matter loss rate	Volumetric grain mass loss due to respiration	kg m^{-3} s^{-1}
Q_r	Heat of respiration	Volumetric heat generation by oxidation	J m^{-3} s^{-1}
C_T	Effective thermal capacity	Volumetric heat capacity of grain–air system	Jm^{-3} °C^{-1}
D_T	Thermal coupling coefficient	Coupling between moisture change and energy storage	J m^{-3}
v_T	Thermal advection coefficient	Convective transport of thermal energy	Jm^{-2} s^{-1} °C^{-1}
S_T	Thermal source term	Volumetric heat generation term	J m^{-3} s^{-1}
C_U	Moisture capacity	Grain bulk density	kg m^{-3}
v_U	Moisture advection coefficient	Convective vapor mass flux	kg m^{-2} s^{-1}
S_U	Moisture source term	Volumetric moisture generation	kg m^{-3} s^{-1}

TABLE A2 | Numerical and discretization parameters.

Symbol	Meaning	Description	Unit
N_y	Number of spatial nodes	Number of grid points in the vertical direction	—
N_t	Number of time steps	Total number of time iterations	—
Δy	Spatial step	Distance between adjacent spatial nodes	m
Δt	Time step	Time increment between iterations	s
P	Central node	Current spatial grid point	—
S	South node	Grid point below P	—
N	North node	Grid point above P	—
n	Time index	Current time level	—
$n+1$	Next time index	Updated time level	—
Co	Courant number	Ratio of advective to storage effects	—
τ	Courant-type parameter	Alternative notation for Co (Leith scheme)	—
μ	Artificial viscosity factor	Dimensionless numerical stabilization parameter	—
σ	Smoothness metric	Measure of numerical oscillations	°C^2

Simulation Parameters and Constitutive Relations

This subsection reports the complete set of simulation inputs used in the numerical experiments presented in the main text. In addition to fixed geometric and operating conditions (e.g., bed height, inlet temperature, airflow velocity), the aeration model requires constitutive relations for thermophysical and psychrometric quantities (e.g., air density, latent heat, and sorption-related parameters). To avoid duplicating derivations already established in prior validated work, all parameters defined through analytical expressions follow the same methodology reported in [14].

TABLE A3 | Constitutive relations and adopted values used in the simulations for soybean.

Variable	Constitutive relation/adopted value	References
t	$t \in [0, 3600]$ s (experimental duration)	[17]
y	$y \in [0, 1]$ m (experimental bed height)	[17]
T_B	31.1°C	[17]
T_I	52.9°C	[17]
U_p	12% (experimental, wet basis)	[17]
u_a	0.23 m s^{-1}	[17]
ρ_a	Analytical expression	[14]
ρ_σ	720 kg m^{-3}	[14]
ε	0.40 (40%)	[51]
c_g	1670 Jkg^{-1} °C^{-1}	[52]
c_W	4186 Jkg^{-1} °C^{-1}	[51]
c_a	1000 Jkg^{-1} °C^{-1}	[51]
h_v	Analytical expression	[14]
h_s	Analytical expression (Chung–Pfost, soybean)	[14]
A	5.68 (soybean)	[14]
B	2.10×10^4 (soybean)	[14]
C	1.34 (soybean)	[14]
$\frac{dm}{dt}$	Analytical expression	[14]
Q_r	15, 778 J m^{-3} s^{-1}	[53]

Unless otherwise stated, the adopted parameter values correspond to those of the experimental soybean aeration study used for validation (Section 2) and are summarized in Table A3. Reporting these inputs explicitly, together with their sources, ensures transparency, traceability, and direct reproducibility of the results.

Appendix B

Origin and Onset of Numerical Oscillations in the Grain-Aeration Model

This appendix presents a diagnostic analysis of the numerical mechanism responsible for the onset of oscillatory behavior observed in the grain-aeration simulations. The objective is to identify (i) the governing operator from which the oscillations originate, (ii) the simulation stage at which they are triggered, and (iii) the parametric dependence controlling their magnitude. To the authors' knowledge, such a time-resolved and operator-level analysis of numerical oscillations in grain-aeration models has not been previously reported in the literature, where oscillatory behavior is typically documented but not explicitly traced back to its advective origin and temporal activation. In this appendix, the simulations are intentionally conducted *without* artificial viscosity ($\mu = 0$).

Advective Origin of the Oscillatory Mechanism

In the one-dimensional formulation adopted in this work, the energy balance equation along the vertical coordinate y can be written in the generic form

$$C_T(T, U)\,\frac{\partial T}{\partial t} + v_T(T, U, u_a)\,\frac{\partial T}{\partial y} \;=\; \mathcal{R}(T, U), \tag{B1}$$

where C_T is the effective volumetric heat capacity, v_T is the advective transport coefficient associated with the aeration airflow, and $\mathcal{R}(T, U)$ collects the remaining coupled contributions (moisture-coupling and source terms) defined in the main text.

The advective coefficient v_T scales linearly with the superficial air velocity u_a. As a consequence, variations in u_a directly modulate the relative strength of the advective operator with respect to the remaining terms in Equation (B1). In finite difference discretizations, the advective operator is the primary source of dispersive truncation errors, which may manifest as nonphysical oscillations when sharp gradients are transported across the grid. By contrast, the remaining terms grouped in $\mathcal{R}(T, U)$ act as storage/coupling and volumetric forcing contributions and do not generate the alternating overshoot–undershoot patterns characteristic of advective dispersion.

A compact, stepwise measure of the discrete advective action is provided by the (time-dependent) Courant number

$$\mathrm{Co}(t) \;=\; \frac{v_T(t)}{C_T(t)}\,\frac{\Delta t}{\Delta y}, \tag{B2}$$

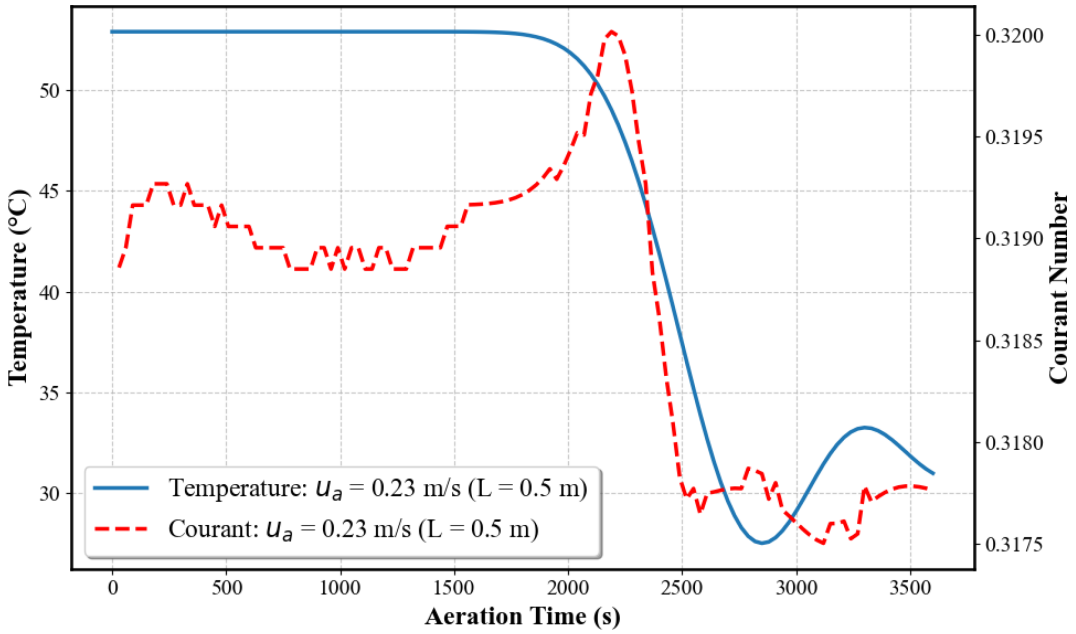

FIGURE B1 | Temporal evolution of temperature and corresponding Courant number at a representative location for $u_a = 0.23$ m s^{-1}. The Courant number attains a local maximum during the passage of the thermal front, indicating a transient increase in the strength of the discrete advective operator. Temperature oscillations emerge shortly after this peak, consistent with the generation of dispersive numerical errors during the transport of sharp gradients.

which is evaluated dynamically using the same coupled coefficients appearing in Equation (B1). Since v_T depends directly on u_a, reducing the aeration velocity leads to an approximately proportional reduction in Co(t) and, therefore, to a systematic weakening of the discrete advective mechanism.

Temporal Onset of Oscillations

Although advection is present throughout the simulation whenever $u_a > 0$, numerical oscillations do not arise uniformly in time. Their onset is confined to a short transient interval associated with the passage of a steep thermal front through the computational domain.

Figure B1 shows the temporal evolution of temperature and the corresponding Courant number at a representative axial location for $u_a = 0.23$ m s^{-1}. During the initial stage of the simulation, the temperature field remains smooth and no oscillatory behavior is observed, despite the presence of advection.

As the thermal front reaches the monitoring location, Co(t) attains a pronounced local maximum. This behavior results from the combined effect of advective transport and the rapid local variation of the coupled thermophysical coefficients embedded in v_T/C_T. During the front passage, steep temperature gradients temporarily amplify the dispersive content of the discrete advective operator, even though the imposed aeration velocity remains constant.

This local Courant peak marks the instant at which the discrete advective operator is most dispersive, maximizing the contribution of non-dissipative truncation errors. The temperature oscillations emerge shortly after this peak, indicating that the oscillatory behavior is generated during the front passage but becomes visible only once the contaminated signal propagates through the numerical stencil. This delayed manifestation is characteristic of dispersive numerical errors and confirms that the oscillations are numerical artifacts rather than physical instabilities of the governing equations.

Quantitative Evidence From an Aeration-Velocity Sweep

To further substantiate the advective origin of the oscillations, a systematic sweep of the aeration velocity u_a was performed while keeping all other physical parameters, initial and boundary conditions, and discretization settings fixed. For each case, the time history of the Courant number and the global temperature oscillation metric were evaluated.

Here, the oscillation metric is taken as the temperature smoothness indicator (Equation (36) in the main text) computed for the temperature field in the unstabilized regime ($\mu = 0$), and is denoted by σ_T. The values reported as 0.00 indicate that σ_T fell below numerical reporting precision in the corresponding runs.

Table B1 summarizes the average and maximum Courant numbers together with the corresponding oscillation metric. Changes are reported relative to the reference case $u_a = 0.23$ m s^{-1}.

TABLE B1 | Effect of aeration velocity on advective strength and temperature oscillations (unstabilized simulations, $\mu = 0$). Changes in σ_T are reported relative to the reference case $u_a = 0.23$ m s^{-1}.

u_a (m s^{-1})	$\overline{\mathrm{Co}}$	$\mathrm{Co}_{\max}$	σ_T	$\sigma_T/\sigma_{T,\mathrm{ref}}$	Change (%)
3.00×10^{-1}	0.415	0.418	37.84	1.315	+31.5
2.30×10^{-1}	0.319	0.320	28.77	1.000	0.0
2.00×10^{-1}	0.277	0.278	23.85	0.829	−17.1
1.50×10^{-1}	0.208	0.209	3.77	0.131	−86.9
1.00×10^{-1}	0.139	0.139	0.00	0.000	−100.0
5.00×10^{-2}	0.069	0.069	0.00	0.000	−100.0
1.00×10^{-2}	0.014	0.014	0.00	0.000	−100.0

The results in Table B1 reveal a clear and nonlinear dependence of the oscillation magnitude on the strength of advective transport. For aeration velocities equal to or greater than $u_a = 0.20$ m s^{-1}, the oscillation metric remains significant and increases with the Courant number. Increasing the velocity from $u_a = 0.23$ m s^{-1} to $u_a = 0.30$ m s^{-1} increases the oscillation metric by 31.5%, consistent with a stronger dispersive advective action.

As the aeration velocity is reduced, a sharp transition is observed. Lowering u_a from 0.23 m s^{-1} to 0.15 m s^{-1} reduces the oscillation metric by approximately 87%, indicating a substantial weakening of the dispersive mechanism. For $u_a \leq 0.10$ m s^{-1}, the oscillation metric collapses to zero within reporting precision, signaling the practical suppression of advectively induced oscillations for the present discretization and operating conditions.

The time-resolved evidence in Figure B1 complements these parametric results by demonstrating that oscillations are generated during short intervals of intense advective transport associated with the thermal-front passage. When the aeration velocity is sufficiently reduced, the Courant peak remains below the threshold required to activate the oscillatory mechanism, explaining the complete disappearance of oscillations reported in Table B1.